SARS-CoV-2 induced CYP19A1 expression in the lung correlates with increased aromatization of testosterone-to-estradiol in male golden hamsters

Stephanie Stanelle-Bertram
Heinrich Pette Institute Hamburg
Berfin Schaumburg
Leibniz Institute for Experimental Virology
Nancy Mounogou Kouassi
Heinrich Pette Institute Hamburg
Sebastian Beck
Heinrich Pette Institute Hamburg
Martin Zickler
Leibniz Institute for Experimental Virology
Georg Beythien
Universtity of Veterinary Medicine, Hannover
Kathrin Becker
University of Veterinary Mediicine Hannover
Tian Bai
Leibniz Institute for Experimental Virology
Hanna Jania
Leibniz Institute for Experimental Virology
Zacharias Müller
Leibniz Institute for Experimental Virology
Vinicius Pinho dos Reis
Leibniz Institute for Experimental Virology
Vanessa Krump-Buzumkic
University for Veterinary Medicine Hannover
Alan Kadek
Leibniz Institute for Experimental Virology
Charlotte Uetrecht
Leibniz Institute for Experimental Virology
Maria Schroeder
University Hospital Hamburg-Eppendorf
Dominik Jarczak

University Hospital Hamburg-Eppendorf
Axel Nierhaus
University Hospital Hamburg-Eppendorf
Stefan Kluge
University Hospital Hamburg-Eppendorf
Pietro Scaturro
Heinrich Pette Institute, Leibniz Institute for Experimental Virology https://orcid.org/0000-0001-9098-3087
Wolfgang Baumgärtner
University of Veterinary Medicine Hannover https://orcid.org/0000-0001-8151-5644
Karin Klingel
University Hospital Tuebingen
Gabriel Guelsah (guelsah.gabriel@leibniz-hpi.de)
Leibniz Institute for Experimental Virology

Biological Sciences - Article

Keywords: Androgens, Sex Bias, Dysregulation of Sex Hormones, Abundant CYP19A1 Expression, Sex-specific Disease Outcome, Complex Metabolic Cross Talk

Posted Date: November 21st, 2020

DOI: https://doi.org/10.21203/rs.3.rs-107474/v1

SARS-CoV-2 infection induced CYP19A1 expression in the lung correlates with increased aromatization of testosterone-to-estradiol in male golden hamsters

Stephanie Stanelle-Bertram[1#], Berfin Schaumburg[1#], Nancy Mounogou Kouassi[1], Sebastian Beck[1], Martin Zickler[1], Georg Beythien[2], Kathrin Becker[2], Tian Bai[1], Hanna Jania[1], Zacharias Müller[1], Vinicius Pinho dos Reis[1], Vanessa Krupp-Buzumkic[3], Alan Kadek[4,5], Charlotte Uetrecht[4,5], Maria Schroeder[6], Dominik Jarczak[6], Axel Nierhaus[6], Stefan Kluge[6], Pietro Scaturro[7], Wolfgang Baumgärtner[2], Karin Klingel[8] and Gülsah Gabriel[1,3]

[1]Department for Viral Zoonoses-One Health, Heinrich Pette Institute, Leibniz Institute for Experimental Virology, Hamburg, Germany; [2]Department of Pathology, University of Veterinary Medicine Hannover, Hannover, Germany; [3]Institute for Virology, University for Veterinary Medicine Hannover, Hannover, Germany; [4]Junior Research Group for Dynamics of Viral Structures, Heinrich Pette Institute, Leibniz Institute for Experimental Virology, Hamburg, Germany; [5]European XFEL GmbH, Schenefeld, Germany; [6]Department of Intensive Care Medicine, University Medical Center Hamburg-Eppendorf, Hamburg, Germany; [7]Junior Research Group for Systems Arbovirology, Heinrich Pette Institute, Leibniz Institute for Experimental Virology, Hamburg, Germany; [8]Institute for Pathology and Neuropathology, University Hospital Tuebingen, Germany;

[#]shared first authorship

correspondence to: guelsah.gabriel@leibniz-hpi.de

Summary

SARS-CoV-2 infection is associated with increased morbidities in men compared to women. Androgens are believed to play an important role in SARS-CoV-2 pathogenesis in men due to the postulated androgen-dependency of ACE2 and TMPRSS2. However, it is yet unclear whether the sex bias is mediated by SARS-CoV-2 infection itself or by other confounding factors. Here, using the golden hamster model, we show that SARS-CoV-2 infection attacks reproductive organs, causes massive dysregulation of sex hormones and induces elevated transcription of the androgen-to-estrogen converting enzyme aromatase CYP19A1 in the lung. In male hamsters, SARS-CoV-2 infection causes severely depleted testosterone and highly elevated estradiol levels. In female hamsters, SARS-CoV-2 infection causes reduced estradiol levels. Hormonal dysregulation in infected animals is followed by severe weight loss compared to control groups treated with poly(I:C) or PBS. Lungs of SARS-CoV-2 infected animals present abundant CYP19A1 expression in the endothelium and in macrophages, particularly in males. Prominent CYP19A1 expression in endothelial cells and macrophages was verified in lung sections of deceased Covid-19 males compared to females. Our results demonstrate that SARS-CoV-2 infection leads to massive dysregulation of sex hormones, which may increase the risk for sex-specific disease outcome particularly in combination with comorbidities. These findings provide insights into the complex metabolic cross talk between SARS-CoV-2 infection and sex hormones.

Introduction

SARS-CoV-2 was first detected in humans in Wuhan, China in November 2019 and was declared a pandemic by the World Health Organization on 11th March 2020. Since, then ~46 million people were diagnosed with SARS-CoV-2 and ~1.1 million died worldwide (as of 1st November 2020). There is accumulating evidence that men are more vulnerable to severe SARS-CoV-2 caused disease (Covid-19) outcome compared to women across countries [1]. A cohort study from the UK with 17 million patients enrolled, identified that being male and older age belongs to the highest risk factors [2]. However, the increased Covid-19 case fatality rate in males is not reflected by increased SARS-CoV-2 male incidence [3-5]. This further highlights the existence of factors that predispose men to an elevated risk to die of Covid-19 compared to women [6]. Another population-based study analyzing data obtained from ~194 million men and ~201 million women across England and Wales, France, Germany, Italy, Netherlands, Portugal, Korea and Spain revealed that the overall male-to-female sex ratio increased in combination with increasing age [7]. Factors that mediate sex disparity in Covid-19 outcome might include a complex interaction of biological sex differences (e.g. chromosomes, sex steroids) or gender aspects (e.g. social behavior) [8]. Sex differences of genetic origin are constant throughout life, while sex differences originating from hormonal effects may alter with increasing age.

To identify the impact of biological sex on SARS-CoV-2 disease outcome, we analyzed the dynamics of sex hormones, sex hormone converting enzymes, viral loads and expression of viral entry factors (ACE2, TMPRSS2) in combination with unbiased lung proteome analysis using the golden hamster model [9,10] reported to reflect major clinical findings, such as systemic spread.

Results

Respiratory SARS-CoV-2 infection disseminates to the reproductive organs of male and female hamsters

In order to assess potential sex differences in SARS-CoV-2 pathogenesis, we intranasally infected male and female hamsters. As controls, animals were intranasally treated with PBS or poly(I:C) as an immune stimulant. Both sexes underwent weight loss upon SARS-CoV-2 infection with a peak drop of ~20% at day 6 p.i. compared to control groups (**Figure 1a** and **b**). Both, male and female hamsters recovered reaching their initial weight on day 14 p.i.. No significant difference was observed in weight loss or recovery time between male and female animals (**Figure 1c**). SARS-CoV-2 replicated to high titers in the lungs of male and female hamsters causing pneumonia with multifocal moderate infiltrates of mononuclear cells and neutrophils unlike PBS or poly(I:C) controls (**Figure 1d, e; Extended Data Figure 1**). Interestingly, replicating SARS-CoV-2 was also detected in the plasma and the gonads (**Figure 1f-o**). In the plasma, replicating virus was detected in 4 out of 5 male animals and in 3 out of 5 female animals (**Figure 1f**). In the testis, 1 out of 5 animals showed replicating virus and 3 out of 5 were viral RNA (vRNA) positive without major pathological changes (**Figure 1g-i**). In the ovaries, 4 out of 5 animals were virus positive and 2 out of 5 animals presented vRNA with no severe pathologies (**Figure 1j-l**). In the light of the infected ovaries, we also assessed whether SARS-CoV-2 could also infect the uterus and found that 2 out of 5 animals were virus positive and 3 out of 5 animals were vRNA positive again without causing major pathological changes (**Figure 1m-o**).

These findings show that SARS-CoV-2 replicates in the organs of the reproductive system of hamsters. No significant difference is detected in weight loss or survival upon SARS-CoV-2 infection between the herein used young and healthy male and female animals without existing comorbidities reflecting clinical reports [2,7].

SARS-CoV-2 infection mediates elevated macrophage inflammatory protein and reduced vascular endothelial growth factor levels in the lungs of male and female hamsters

We then studied sex-dependent local and systemic innate immune responses of SARS-CoV-2 infected hamsters compared to PBS and poly(I:C) treated control animals at various time points after infection. We analyzed a panel of 13 different cytokines and chemokines (eotaxin, MIP-1α, MIP-1β, IFN-γ, IL-2, IL-6, IL-10, IL-12, IL-13, IL-1β, MCP-1, TNF-α and VEGF). In the

lung, on day 1 p.i., infected groups did not show significant cytokine/chemokine induction except for poly(I:C) treated males and females for MIP-1α and MIP-1β (**Extended Figure Data 2a-k**). On day 3 p.i. in the lung, IL-6, IL-1ra, Eotaxin and MIP-1α levels were significantly increased in infected male and female animals as compared to uninfected control groups (**Figure 2a-e**). IFN-γ levels were higher in female SARS-CoV-2 infected animals compared to males, albeit the intrinsic IFN-γ levels were already elevated in the lungs of PBS treated groups (**Figure 2f**). Interestingly, VEGF was the only cytokine within the panel assessed that was significantly reduced in SARS-CoV-2 infected male and female hamsters compared to uninfected controls (**Figure 2g**). All other cytokines and chemokines did not show any significant alterations between groups and sexes, albeit IL-10 and IL-12 levels seemed to be slightly reduced in infected female hamsters as compared to the respective PBS or poly(I:C) controls (**Figure 2h-o**). On day 6 p.i., most altered cytokines and chemokines in the infected groups were again comparable to the uninfected controls in both sexes (**Extended Data Figure 2l-s**). However, eotaxin and MIP-1α levels were still highly elevated in the lungs of SARS-CoV-2 infected male and female hamsters (**Extended Data Figure 2l, m**). MIP-1β levels that were unaltered on day 3 p.i., showed high levels on day 6 p.i. in infected hamsters. VEGF levels remained strongly reduced in the lungs of SARS-CoV-2 infected male and female animals even on day 6 p.i. (**Extended Data Figure 2o**). In the plasma, however, most cytokines and chemokines assessed did not show major differences among all groups with the exception of slightly reduced eotaxin levels at day 6 p.i. in infected females (**Extended Data Figure 3**).

These findings show that SARS-CoV-2 infection mediates inflammatory cytokine responses mainly occur in the lungs of male and female hamsters. In particular, a strong induction of macrophage secreted inflammatory chemokines MIP-1α and MIP-1β levels correlates with suppressed VEGF levels that is involved in vascular wound repair processes.

SARS-CoV-2 infection mediates reduced testosterone and increased estradiol levels in the plasma of male hamsters

Infectious SARS-CoV-2 particles were detected in the gonads of infected animals, where major sex hormones are produced and then secreted into the blood system. Thus, any changes in systemic sex hormone responses would have implications on immune responses given the presence of androgen and/or estrogen receptors on the surface of most immune cells [11]. Therefore, we measured the major sex hormones in the plasma of SARS-CoV-2 infected animals in comparison to uninfected controls treated with PBS or poly(I:C) at multiple time

points after infection to allow identification of potential dynamic processes. Testosterone levels in the plasma of SARS-CoV-2 infected male hamsters were significantly reduced on day 3 p.i., started to recover on day 6 p.i. and fully recovered on day 14p.i. to comparable levels of uninfected control groups treated with PBS or poly(I:C) (**Figure 3a**). Testosterone levels in the plasma of SARS-CoV-2 infected female hamsters were similarly low among all infected and uninfected groups and likely not allowing the detection of potential alterations (**Figure 3b**). Estradiol levels were significantly elevated in SARS-CoV-2 infected male hamsters on day 3 p.i. with still high levels on day 6 p.i. and fully recovered levels on day 14 p.i. compared to uninfected control groups (**Figure 3c**). Estradiol levels in infected female hamsters on the other hand were significantly reduced on day 3 p.i. compared to uninfected controls, while on day 6 and 14 p.i. estradiol levels were again comparable among all groups (**Figure 3d**). Cortisol levels in the plasma of SARS-CoV-2 infected male and female hamsters were elevated on day 3 and 6 p.i. normalizing back on day 14 p.i. likely due to infection stress (**Figure 3e, f**). Progesterone levels were slightly elevated on day 3 but not 6 or 14 days p.i. in SARS-CoV-2 infected male and female hamsters unlike their respective negative controls (**Figure 3g, h**).

Importantly, we included additional control groups to see whether any respiratory viral infection would mediate reduced testosterone and increased estradiol levels in the plasma. Therefore, we used a 2009 pandemic H1N1 influenza A virus (pH1N1) isolate and an avian H7N9 influenza A virus isolated from a patient. Both, pH1N1 and H7N9 influenza virus infections mediated low testosterone levels upon infection but did not alter estradiol levels in male mice in line with previous reports [12]. Thus, the shift in sex hormones from testosterone-to-estradiol detected seems to be specific for SARS-CoV-2 infection in male animals (**Extended Data Figure 4**).

These findings show that SARS-CoV-2 infection mediates severe dysregulation of sex hormones. In infected males, reduced testosterone levels are paralleled with increased estradiol levels unlike in infected females.

SARS-CoV-2 infection in the lung correlates with reduced ACE2 and TMPRSS2 transcription

Both SARS-CoV-2 entry factors, ACE2 and TMPRSS2 possess postulated androgen receptors [13,14] giving rise to the discussion whether testosterone levels in males might determine SARS-CoV-2 disease outcome. Therefore, we measured the transcription levels of ACE2 and

TMPRSS2 as well as controls including DPP4, ACE and the androgen receptors AR and ZIP9. In the lung, ACE2 mRNA levels in SARS-CoV-2 infected male and female animals were unaffected on day 1 p.i., became significantly reduced on day 3 p.i. and were further reduced on day 6 p.i. (**Figure 3i-k**). Transcription levels of ACE, a homologue of ACE2, in the lung, were not affected (**Figure 3l**). Interestingly, ACE2 transcription was not impaired in the testis or in the ovaries (**Figure 3m and n**). In the lung, a similar trend was detected with DPP4, the MERS-CoV receptor, and TMPRSS2 resulting in significantly reduced DPP4 and TMPRSS2 levels (**Figure 3o-q**). In contrast, transcription levels of the internal (AR) or membrane-bound (ZIP9) androgen receptors were not changed (**Figure 3r and s**).

These findings show that reduced transcription levels of ACE2 and TMPRSS2 correlate with reduced testosterone levels on day 3 p.i. However, transcriptional levels still remain reduced on day 6 p.i., albeit testosterone levels already start to recover on day 6 p.i.. This observation is in line with previous reports on ACE2 and TMPRSS2 downregulation in SARS-CoV infected cells [15-17]. These data might suggest that the transcription of SARS-CoV-2 entry factors might not be exclusively controlled by testosterone.

SARS-CoV-2 infection in the lung is not associated with major differences between sexes

Data obtained so far indicate that cytokine and chemokine induction upon SARS-CoV-2 infection mainly occurs in the lung. Thus, we wanted to identify potential cellular factors that might mediate severe lung pathology in infected male and female animals. Therefore, we used an unbiased proteomic approach. Herein, protein levels were quantified in the lungs of hamsters infected with SARS-CoV-2 or control groups treated with PBS or poly(I:C), respectively. Expression of various cellular proteins changed in SARS-CoV-2 infected animals compared to uninfected control groups (**Extended Data Figure 5 and 6**). However, only three cellular proteins were detected that significantly differ between males and females upon SARS-CoV-2 infection (**Figure 4**). In infected females, the Golgi SNARE protein and the Ig-like domain-containing protein were expressed to significantly higher levels compared to infected males. Interestingly, serum amyloid A-5 protein was expressed to significantly higher levels in infected males compared to females. Serum amyloid A protein is an acute-phase protein, that is stimulated by pro-inflammatory cytokines (IL-6, IL-2, TNF-α, IFN-γ and TGF) and released in response to general inflammation [18]. The identification of limited factors that are significantly altered between males and females upon SARS-CoV-2 infection suggests that other or additional factors might be responsible for the increased vulnerability of males to Covid-19.

SARS-CoV-2 infection induces increased aromatase CYP19A1 transcription in the lung but not in the gonads

Since data obtained from the unbiased proteomics analysis revealed no major differences in altered protein levels between males and females, we focused on the dysregulation of sex hormones and its potential underlying mechanisms. Reduced testosterone and elevated estradiol levels in males indicate altered aromatization. The conversion of testosterone-to-estradiol occurs via the aromatase CYP19A1, which is expressed in a wide range of tissues (including gonads and the lung) but also in endothelial cells and in the vascular wall in humans and various mammalian species [19-22]. The aromatase CYP19A1 gene contains predicted binding sites for key transcription factors, such as estrogen receptor, progesterone receptor, androgen receptor, C/EBP-α (CCAAT-enhancer binding protein α; mainly involved in myeloid differentiation), SF-1 (steroidogenic factor-1; involved in sex determination by controlling activity of genes related to the reproductive glands or gonads and adrenal glands), NFAT-1/-2 (a regulator of T-cell response), IRF-1,-3 (controls expression of various cytokines), C-ets-1 (controls the expression of cytokine and chemokine genes), FOXP3 (involved in regulatory T-cell function), STAT1,-3,-4,-6 (regulators of various aspects of cellular immunity) and NF-κB (regulates genes responsible for innate and adaptive immune response) [23-27] indicating a key role in reproduction and immunity (**Figure 5a**). Thus, we first assessed whether SARS-CoV-2 infection mediated induction of cytokines and chemokines in the lung may alter aromatase CYP19A1 transcription. Since the CYP19A1 gene of the golden hamster is not fully sequenced, we first sequenced regions of the gene and designed specific primers (data not shown). Lack of availability of full genome sequences of the golden hamster model might reflect one limitation of the proteome analysis. Interestingly, we could detect significantly elevated aromatase CYP19A1 mRNA levels starting on day 3 p.i. in SARS-CoV-2 infected males and females, albeit levels were slightly higher in males as compared to the control groups treated with PBS or poly(I:C) (**Figure 5b and c**). CYP19A1 mRNA levels remained elevated, particularly in males, on day 6 p.i. (**Figure 5d**). To exclude that also other sex hormone converting enzymes might be affected upon SARS-CoV-2 infection in the lung, we assessed mRNA levels of the 5-α reductase as a control, which converts testosterone-to-dihydrotestosterone. Transcription levels of 5-α reductase were not affected in the lungs of SARS-CoV-2 infected male or female hamsters compared to the PBS and poly(I:C) control groups (**Figure 5e**). Since the CYP19A1 aromatase is also expressed in the gonads, we analyzed its expression in the testis and ovaries of infected versus uninfected animals. CYP19A1 aromatase mRNA levels were not altered in the testis or ovaries upon SARS-CoV-2 infection as compared to the control treatments (**Figure**

5f and g). This suggests that CYP19A1 aromatase is dysregulated in the lung upon SARS-CoV-2 infection, particularly in males. Since estradiol plays a key role in endothelial function and angiogenesis, we wanted to know whether endothelial activation might be detected in the lung. Therefore, we measured levels of endothelial lipase, which is secreted by vascular endothelial cells and is involved in metabolic disorders [28,29]. Herein, we detected significantly elevated endothelial lipase levels in males, albeit a non-significant increase was also detected in females upon SARS-CoV-2 infection on days 3 and 6 p.i. compared to uninfected controls treated either with PBS or poly(I:C) (**Figure 5h and i**).

These findings suggest that transcription of the CYP19A1 aromatase gene is specifically up-regulated in the lungs of SARS-CoV-2 infected animals correlating with endothelial activation, particularly in males.

Aromatase CYP19A protein is abundantly expressed in perivascular and peribronchiolar infiltrates of male hamsters infected with SARS-CoV-2

We then wanted to identify, which cell types in the lung express the CYP19A aromatase. Therefore, we stained serial lung sections of male and female hamsters either infected with SARS-CoV-2 or uninfected controls treated with PBS or poly(I:C), respectively. CYP19A aromatase expression was directly compared to serial sections stained with markers for cell types known to express aromatase, such as the endothelium (CD31, vWF) and smooth muscle cells (SMA). In addition, we used markers to detect immune cells (CD204, CD3) and viral NP (**Figure 6; Extended Data Figure 7**). To assess expression levels in different tissues, the aromatase immunoreactivity was scored semiquantitatively in the bronchiolar epithelium, the endothelium and the peribronchiolar as well as perivascular regions of the lung sections. All groups showed CYP19A1 aromatase expression in endothelial cells, bronchiolar epithelium as well as perivascular connective tissue, whereas peribronchiolar expression was only present in poly(I:C) treated and in infected animals (**Figure 6**). Male PBS treated controls showed an overall low immunoreactivity of CYP19A aromatase in bronchiolar epithelium, endothelial cells and perivascular connective tissue (**Figure 6a**). Female PBS treated control animals showed only very low reactivity in respective tissues (**Figure 6b**). Poly(I:C) treated controls and infected animals showed an especially high level of immunoreactivity in perivascular connective tissue, beside the additional expression of CYP19A aromatase in peribronchiolar tissue (**Figure 6**). The perivascular as well as the peribronchiolar tissue was both infiltrated by moderate amounts of macrophages (CD204-positive) and low amounts of T-lymphocytes

(CD3-positive). In both sexes, expression was considerably higher in infected animals than in poly(I:C) controls. Male individuals showed substantially higher expression than females (**Figure 6**).

Thus, histological findings in the golden hamster model indicate that CYP19A1 protein is expressed to higher amounts in the male compared to the female lung upon SARS-CoV-2 infection.

Aromatase CYP19A1 protein is abundantly expressed in endothelial cells and macrophages of fatal male Covid-19 cases

To see whether increased CYP19A1 aromatase expression detected in the hamster model can be translated into the clinical setting, we stained lung sections obtained from seven deceased Covid-19 patients (four males and three females) as well as negative controls against the CYP19A1 aromatase. All Covid-19 patients presented CYP19A1 positive cells in their lungs (**Figure 7a-h**). CYP19A was expressed in endothelial cells and particularly in macrophages around major areas of inflammation. Interestingly, a significantly higher expression of CYP19A1 was observed in macrophages and endothelial cells in all male compared to female Covid-19 patients or control patients without lung disease. In a semiquantitative score judging the intensity of signals in CYP19A positive cells (0-3) we found in males (n=4, 3 +/- 0, in females n=3, 2 +/- 0 and in control patients (n=3, 1 +/- 0).

To assess whether CYP19A1 induction is mediated by viral infection directly, we infected *ex vivo* human lung cultures (Calu-3) with SARS-CoV-2 and pH1N1 influenza as a control. We could detect significantly elevated CYP19A1 transcription levels upon SARS-CoV-2 infection unlike H1N1 infection or PBS treated controls (**Figure 7i**).

These findings suggest that SARS-CoV-2 infection specifically induces elevated CYP19A1 transcription in the lung. Histological findings from Covid-19 cases further show that CYP19A1 protein is most abundantly expressed in macrophages of deceased men compared to women.

Discussion

Our results in the golden hamster model revealed key differences in sex hormone levels upon SARS-CoV-2 infection that might play an important role in sex-specific disease outcome, particularly in combination with other comorbidities. First, SARS-CoV-2 replicates in reproductive organs likely leading to impaired sex hormone production, which might affect paracrine functions (**Extended Data Figure 8**). Second, we found that in males unlike in females, systemic reduction of testosterone levels is accompanied by elevated estradiol levels, which might additionally affect endocrine functions of the sex hormones. Control male animals infected with H1N1 and H7N9 influenza A virus presented reduced testosterone levels as shown before but not elevated estradiol levels [12]. This is in line with findings from human cohorts, where H1N1 and H7N9 influenza A virus infection in men correlated with low testosterone but not elevated estradiol levels [30]. This is also in agreement with our previous report that critically ill male Covid-19 patients present low testosterone and high estradiol levels [31]. In contrast to the findings here in the hamster model, critically ill female patients presented not reduced but elevated estradiol levels combined with elevated testosterone levels [31]. However, it should be considered that 10 out of 11 critically ill Covid-19 women analyzed in the above mentioned study [31] were postmenopausal in contrast to the young female animals used in this study. Current studies further highlight that the menstrual status in women may affect Covid-19 outcome suggesting that more investigation is needed in pre- and postmenopausal females to understand the impact of female hormones on female pathogenesis [32]. Third, we show that transcription and expression of the CYP19A1 aromatase, which is responsible for the conversion of testosterone-to-estradiol is elevated in the lungs of SARS-CoV-2 infected animals, particularly in males. Indeed, previous reports also showed that CYP19A1 aromatase is detected to higher levels in male animals and humans compared to their female counterparts [33]. Elevated CYP19A1 levels in the lung of SARS-CoV-2 infected male hamsters correlate with significantly increased levels of endothelial lipase, which is an endothelial activation marker involved in metabolic disorders [28,29]. Histochemical analysis revealed that CYP19A1 is expressed to particular high levels in the perivascular region, including macrophages of infected male compared to female hamsters. It was proposed that the immunological hyper-response, characterized by widespread endothelial damage, complement-induced blood clotting and systemic microangiopathy play critical roles in Covid-19 exacerbation [34]. Endothelial activation and the complement system are highly debated as playing important roles in severe SARS-CoV-2 disease outcome in humans [35]. CYP19A1 was shown before to be highly expressed in macrophages and proposed to be sufficient for aromatization of estradiol levels from

testosterone to promote cell proliferation, auto-regulate cytokine production and thus fuel inflammation processes [36]. Macrophages express androgen and estrogen receptors that may regulate their activation and thus contribute to sex-specific immune responses [37]. CYP19A1 plays a key role in breast cancer and many clinical trials have shown the efficacy of aromatase inhibitors in the management of breast cancer [38]. Herein, particularly estradiol is a known promoter of vascular inflammation and inhibition of the aromatase was shown to reduce vascularization and formation of metastasis. In line with this observation, it was shown in murine models that mice lacking the CYP19A1 gene are not able to fully repair lung damage compared to mice expressing a functional CYP19A1 gene [39]. Finally, CYP19A1 expression was detected in endothelial cells and macrophages of seven deceased Covid-19 patients. CYP19A1 expression was more pronounced in male than female patients. Macrophages and the macrophage activation syndrome were repeatedly proposed to play a key role in lung inflammation and endothelial damage in Covid-19 patients [40,41].

Collectively, our findings suggest that increased expression of CYP19A1 in the lung upon SARS-CoV-2 infection promotes elevated aromatization and thus likely mediates reduced systemic testosterone and elevated estradiol levels in males. Active SARS-CoV-2 replication in the testis additionally impairs testosterone production in males. Thus, lack of systemic and local testosterone levels in males might result in lack of induction of androgen receptor containing immune cells required to combat viral infection. An additional increase in systemic and local estradiol levels in males might additionally fuel up inflammatory processes via estrogen receptor containing immune cells and their activation, e.g. macrophages (**Extended Figure 9**). It should be further noted that increasing age in men as well as comorbidities with endothelial involvement, such as cardiovascular diseases, adipositas and type II diabetes are associated with hypogonadism (reduced testosterone levels). In cardiovascular diseases [42], adipositas [43,44] and type II diabetes [45] low testosterone levels may be combined with high estradiol levels due to increased aromatase activity. Thus, it is tempting to speculate whether multiple testosterone level reducing and/or estradiol level increasing hits might contribute to severe and even fatal Covid-19 outcome in men. Future studies are required to understand the impact of sex hormones on SARS-CoV-2 pathogenesis in comorbidity models.

Materials and Methods

Viruses

The SARS-CoV-2 strain (SARS-CoV-2/Germany/Hamburg/01/2020; ENA study PRJEB41216 and sample ERS5312751) was isolated by inoculation of VeroE6 cells with 200 µl of a human nasopharyngeal swab of a confirmed patient with Covid-19 in Hamburg and propagated for three serial passages in VeroE6 cells. VeroE6 were cultivated in DMEM (Sigma-Aldrich GmbH) with 2 % fetal bovine serum, 1 % penicillin-streptomycin and 1 % L-glutamine at 37°C for virus propagation. The H7N9 avian influenza A virus (A/Anhui/1/13) and 2009 pandemic H1N1 influenza A virus (A/Hamburg/NY1580/09; pH1N1) were grown and titrated in MDCK II cells. MDCK II cells were cultivated in MEM (Sigma-Aldrich GmbH) with 0,2 % bovine serum albumin (BSA), 1 % penicillin-streptomycin and 1 % L-glutamine at 37°C. All cells were tested negative for Mycoplasma sp. by PCR. All infection experiments with SARS-CoV-2 and H7N9 influenza A virus were performed in the biosafety level 3 (BSL-3) laboratory at the Heinrich Pette Institute, Leibniz Institute for Experimental Virology in Hamburg, Germany.

Animal experiments

Male and female golden hamsters (8-10 weeks old) were purchased from Janvier and male C57BL/6 mice (8 weeks old) were purchased from Envigo. All animals were kept under standard housing conditions (21 ± 2 °C, 40–50% humidity, food and water ad libitum) with a 12:12 light–dark cycle at the Heinrich Pette Institute, Leibniz Institute for Experimental Virology in Hamburg, Germany. For SARS-CoV-2 infection, hamsters were anaesthetized with 150 mg/kg ketamine and 10 mg kg^{-1} xylazine by intraperitoneal injection. The animals were intranasally inoculated with 10^5 plaque forming units (p.f.u.) SARS-CoV-2, mock infected with PBS or were administered with 1 mg kg^{-1} poly(I:C). Body weight was monitored daily up to 14 days post infection (d p.i.). On day 1, 3 and 6 p.i., five animals per group were euthanized by intraperitoneal injection of an overdosis of pentobarbital. Blood was drawn by cardiac puncture and collected in EDTA tubes. Blood was centrifuged for 10 min at 2,000 g and 4 °C, and the plasma was stored at −80 °C. Lungs and gonads were homogenized in 1x PBS and stored at -80 °C. For histopathological examination, lungs and gonads were fixed by immersion in 10% neutral-buffered formalin and embedded in paraffin. For total RNA isolation, lungs and gonads were incubated in RNAprotect Tissue Reagent (QIAGEN), for at least 24 hours at 4 °C and stored at –80 °C.

For influenza A virus infection, mice were anaesthetized with 100 mg kg^{-1} ketamine and 10 mg kg^{-1} xylazine by intraperitoneal injection. The animals were intranasally inoculated with 10^5 p.f.u. H7N9 avian influenza A virus (A/Anhui/1/13), 10^4 p.f.u. pH1N1 influenza A virus (A/Hamburg/NY1580/09) or mock infected with PBS. Body weight was monitored daily. On day 3 p.i., four or five animals per group were anesthetized with isoflurane and blood was drawn by the retrobulbar route and collected in EDTA tubes. Blood was centrifuged for 10 min at 2,000 g and 4 °C, and the plasma was stored at -80 °C.

All animal experiments were performed in strict accordance with the guidelines of German animal protection law and were approved by the relevant German authority (Behörde für Gesundheit und Verbraucherschutz; protocols N 32/2020 and 01/15).

Histology and immunhistochemistry

Tissues were routinely embedded in paraffin and evaluated via light microscopy of hematoxylin and eosin (HE) stained slides. Immunohistochemical detection of SARS-CoV-2 nucleoprotein (NP) aromatase, cluster of differentiation (CD204), von-Willebrandt-factor (vWF), cluster of differentiation 31 (CD31), cluster of differentiation 3 (CD3) and smooth muscle actin (SMA) in the golden hamster lungs was performed using the EnVision+ System (Dako Agilent Pathology Solutions). Serial sections of tissue were dewaxed and rehydrated in isopropanol and 96% ethanol followed by blockage of endogenous peroxidase by incubation in 85% ethanol with 0.5% H_2O_2 for 30 min at room temperature. Antigen retrieval was performed by incubation in citrate (10 mM citric acid, 0.05% Tween 20) or citrate-Na_2H_2EDTA buffer (10 mM citric acid, 2 mM Na_2H_2EDTA, 0.05% Tween 20) for 20 min in a microwave at 800 W, followed by 20 min at room temperature. Sections were afterwards transferred to Shandon Coverplates™ (Thermo Electron GmbH) and stained with either polyclonal antibodies directed against aromatase (Abcam, ab18995, 1:500), CD31 (Acris, AP15436PU, 1:100), CD204 (Abnova Corporation, MAB1710, 1:500) and von-Willebrandt-Factor (Dako Agilent Pathology Solutions, 20051017, 1:500) or monoclonal antibodies against smooth muscle actin (Dako Agilent Pathology Solutions, 20071964, 1:100), CD3 (Dako Agilent Pathology Solutions, A0452, 1:100) and SARS-CoV-2 NP (Sino Biological, 40143-MM05, 1:32,000) over night at 4°C. Antibodies were diluted in PBS containing 1% BSA with and addition of 0,3% Triton X-100 for the aromatase, smooth muscle actin and SARS-CoV-2 NP stainings. Sections were subsequently rinsed, and the peroxidase-labeled polymer was applied as secondary antibody for 30 minutes. Visualization of the reaction was accomplished by incubation in chromogen 3,3-diaminobenzidine tetrahydrochloride (DAB, 0.05%) and 0.03% H_2O_2 in 1x PBS for 5 min and

afterwards counterstained with Mayer's hematoxylin for 1 min. For negative controls, the primary antibody was replaced by either rabbit normal serum (1:3,000) or ascites fluid from Balb/c mice (1:1,000). The serial stainings were afterwards analyzed by light microscopy.

Aromatase immunoreactivity was scored semiquantitativley in the bronchiolar epithelium, the endothelium and the peribronchiolar as well as perivascular regions of the lungs. Signal intensity in respective regions was very low (0,5), low (1), low to moderate (2), moderate (3), moderate to high (4), or high (5). Signal distribution was assessed as: focal/oligofocal (≤3 foci; 1), multifocal (>3 foci; 2) and diffuse (3). For better compararive interpretation a final score for each region and animal was calculated as product of signal intensity times signal distribution.

For immunohistochemical detection of aromatase in lungs of deceased Covid-19 patients lung tissue probes were fixed in 4% phosphate-buffered formaldehyde and embedded in paraffin. Immunohistochemical analysis was performed by using the polyclonal antibody directed against aromatase (Abcam, ab18995, 1:400) on an automated immunostainer following the manufacturer's protocol (Benchmark; Ventana Medical Systems, Tucson, AZ) and using the ultraView detection system (Ventana) and diaminobenzidine as substrate. Tissue sections were counterstained with hematoxylin. For all deceased patients, informed consent had been obtained from the next of kin [46].

Determination of viral titers and viral RNA levels

Homogenization of organs was performed in 1 ml 1x PBS with 5 sterile, stainless steel beads (Ø 2 mm, Retsch) at 30 Hz for 10 min in the mixer mill MM400 (Retsch). The plaque assays were performed on VeroE6 cell monolayers and stained with crystal violet after 72 hours. The tissue homogenisates or plasma were titrated on VeroE6 cells in 10-fold serial dilutions for 30 min at 37°C and overlaid with MEM (Sigma-Aldrich) supplemented with 0,2 % BSA, 1% L-glutamine, 1% penicillin-streptomycin, 1 µg ml^{-1} L-1-tosylamido-2-phenylethyl chloromethyl ketone (TPCK) treated trypsin (Sigma-Aldrich) and 1,25% Avicel. After 72 hours p.i., cells were fixed with 4% paraformaldehyde and the plaques were visualized by crystal violet staining.

Viral RNA was isolated from plasma or homogenized organs using the QIAamp Viral RNA Mini Kit (QIAGEN) according to the manufacturer's instructions. SARS-CoV-2 RNA levels were then determined by quantitative reverse transcription real-time PCR (qRT-PCR) using the RealStar® SARS-CoV-2 RT-PCR Kit RUO (altona Diagnostics). An internal control provided

by the kit was used as a sample preparation control as well as an extended dry spin step for 10 min at 17000g at room temperature.

Measurement of hormone and cytokine levels

Hormone levels were measured in homogenized testis and ovaries as well as in plasma samples using a custom-made MILLIPLEX MAP Multi-Species Hormone Magnetic Bead Panel (Merck), analyzing testosterone, cortisol and progesterone according to the manufacurer's instructions in a Bio-Plex 200 System with high-throughput fluidics (HTF; Bio-Rad). Estradiol levels (Calbiotech) in homogenized testis and ovaries as well as plasma samples were analyzed by ELISA following the manufacturer's instructions. ELISAs were measured on an Infinite M Nano ELISA microplate reader (Tecan). Female hamsters in diestrus were excluded from estradiol anaylsis.

A panel of 13 cytokines and chemokines (eotaxin, macrophage inflammatory protein 1α and 1β (MIP-1α, -1β), interferon-γ (IFN-γ), interleukin-2 (IL-2), interleukin-6 (IL-6), interleukin-10 (IL-10), interleukin-12 (IL-12(p70)), interleukin-13 (IL-13), interleukin-1β (IL-1β), monocyte chemoattractant protein-1 (MCP-1), tumor necrosis factor-α (TNF-α), and vascular endothelial growth factor (VEGF)) was measured in homogenized lungs and plasma using a custom-made Bio-Plex Pro™ Mouse Cytokine multiplex (Bio-Rad) according to the manufacturer's instructions in a Bio-Plex 200 System with high-throughput fluidics (HTF; Bio-Rad).

Infection of Calu-3 cells with SARS-CoV-2

Calu-3 cells (ATCC) were seeded in 6-well plates. After 24 hours Calu-3 cells were infected with SARS-CoV-2 or pH1N1 at a multiplicity of infection (MOI) of 1 in 500 µl DMEM with 1% P/S, 1% L-glutamine and 2% FCS or DMEM with 1% penicillin-streptomycin, 1% L-glutamine and 0.4% BSA, respectively, for 45 min at 37° C. After washing twice with 1x PBS, 2 ml of infection medium DMEM with 1 % penicillin-streptomycin, 1 % L-glutamine and 2 % FCS or DMEM with containing 1 % penicillin-streptomycin, 1 % L-glutamine, 0.1 % FCS and 1 µg/ml TPCK-treated Trypsin (Sigma-Aldrich GmbH) were added and the cells were incubated for 24 hours at 37 °C.

Determination of cytokine, receptor and protease expression levels by real-time quantitative PCR (RT-qPCR)

RNAprotect-fixed lungs were homogenized in 700 µl lysis buffer RL with 5 sterile, stainless steel beads (Ø 2 mm, Retch) at 30 Hz for 10 min in the mixer mill MM400 (Retsch). Calu-3

cells were lysed in 1 ml TRIZOL (Invitrogen) per well, incubated for 5 min at RT. The cell lysate were resuspended and transferred into a fresh tube. 250 µl chloroform were added to each sample, vortexted for 30 sec and subsequently centrifuged for 15 min at 13,000 g. Total RNA was isolated from homogenized tissues and the aqueous phase of the lysed Calu-3 cells using the innuPREP RNA Mini Kit 2.0 (Analytik Jena) according to the manufacturer's instructions with an additional DNase I treatment using the RNase-free DNase Set (QIAGEN). The RNA was eluted in RNase-free water and mixed with 1 U μl^{-1} RiboLock RNase inhibitor (Thermo Fisher Scientific). The cDNA synthesis was performed using random nonamer primers (Gene Link, pd(N)9, final concentration: 5 µM), SuperScript III Reverse Transcriptase (Thermo Fisher Scientific) according to the manufacturer´s instructions and 2 µg total RNA. The cDNA was generated using the GeneAmp PCR System 9700 (Applied Biosystems; cycle: 25 °C for 5 min, 50 °C for 60 min, 70 °C for 15 min, 4 °C hold). Reactions were set up with PCR grade Water (Roche) in LightCycler® 480 Multiwell Plate 96 Reaction Plates (Roche). Briefly, 2 µl of cDNA template were added to 10 µl FastStart Essential DNA Green Master (Roche) and 300 nM of forward and reverse primer, respectively. RT-qPCR runs were conducted using LightCycler® 96 Real-Time PCR System (Roche) with endpoint fluorescence detection: 10 min at 95 °C and 45 amplification cycles (15 s at 95 °C, 10 s at 65 °C and 20 s at 72 °C). Analysis was performed in duplicates for each gene. Negative controls and sample without reverse transcriptase were included to detect contaminations. Relative expression values were determined using a modified $e^{-\Delta\Delta Ct}$ method. Ct values of each samples were normalized to Ct values of the reference gene of the respective sample and the average of the ΔCt value (n = 2 technical replicates) was determined. Hprt1 was used as a reference gene for analyses of mRNA expression levels in the lung and Ywhaz was used reference gene for analyses of mRNA expression levels in the gonads. The relative $2^{-\Delta Ct}$ expression values of the biological replicates are presented. The following primer sequences were used for RT-qPCR: Hprt1 (Hypoxanthin phosphoribosyltransferase 1) forward 5'-TCCCAGCGTCGTGATTAGTG-3', reverse 5'-GTGATGGCCTCCCATCTCTT-3'; Ywhaz forward 5'-AGCCTTTGTCTGCCTCACTC-3', reverse 5'- AAGTTAACTGGCTCTACTCCCC-3', IL-6 forward 5'-TCACCTCTGGTCTTCTGGACT-3', reverse 5'-TCTGGACCCTTTACCTCTTGTT-3' IL-1rα forward 5'-ATGGAAATCTGCAGGGGACG-3', reverse 5'-TAGCCGGCAATGAGTTGGTT-3'; Eotaxin forward 5'- AGAGAGCCTGAGACCAACAC-3', reverse 5'-AACTGGGATAGAGCCTGGGTG-3'; IFN-γ forward 5'-ATGGAGGGGACCTCGTCTTT-3', reverse 5'-GATGGCCTGGTTGTCCTTCA-3'; VEGF forward 5'-CTCCACCATGCCAAGTGGTC-3', reverse 5'-TCTCATCGGGGTACTCCTGG-

3’; ACE2 forward 5’-CAGAGGGAGCAGATGGCTAC-3’, reverse 5’-CCCACATGTCACCAAGCAAA-3’; ACE forward 5’-TCGCCCATCTTAACGGCTAC-3’; reverse 5’-ATCCAGGTTGATGTGCTGGG-3’; TMPRSS2 forward 5’-ACCACCACACTGATCACAGC-3’, reverse 5’-TAGAGGTCGATGTTGCCTGC-3’; DPP4 forward 5’-AAGGCAGGAGCTGTGAATCC-3’, reverse 5’-ACCCATGCCACATCACACAA-3’; AR forward 5’-GGCCTTACCTGGATTCCGC-3’, reverse 5’-AGAGCATCCTGGAGTTGACG-3’; ZIP9 (Slc39a9) forward 5’-CCCTTGTACTGGGCTTCGTT-3’, reverse 5’-CTGCTCCCAAAGCTACACCA-3’; CYP19A1 aromatase forward 5’-ATGCGGCACATCATGCTGAA-3’, reverse 5’-TCTTTCAAGTCCTTGGCGGAT-3’; 5-α reductase 3 forward 5’-ACCCGGGGAAACAGGATACA-3’, reverse 5’- GAACAGGGCAAACACTCCAC-3’; endothelial lipase forward 5’-GAAACCCAGCGCAAACTGAC-3’, reverse 5’-TGAGGTCTTCCGTCAAGTGC-3’; ribosomal protein L32 (RPL32; human) forward 5’-GAAGTTCCTGGTCCACAACG-3’, reverse 5’-GCGATCTCGGCACAGTAAG-3’;.CYP19A1 aromatase (human) forward 5’-CGGCCTTGTTCGTATGGTCA-3’, reverse 5’-CAGAAGGGTCAACACGTCCA-3’;.

Proteomic analysis

Sample preparation. Lungs homogenates were incubated with 4% SDC, boiled 10 min at 98 °C, and sonicated (4 °C for 15 min). Fifty micrograms of cleared protein lysates were reduced/alkylated (10 mM TCEP, 40 mM chloroacetamide) for 1h, and digested overnight with LysC and Trypsin (1:50 w/w proteases:substrate ratio). Peptides were purified on stage tips with two SDB-RPS Empore filter discs (3M, Maplewood, MN, USA) and resuspended in 0.3% ACN/0.3%TFA to a final concentration of 250 ng/µl.

UHPLC and timsTOFpro settings. Samples were analyzed on a nanoElute (framework V1.1.0.63; Bruker, Germany) coupled to a timsTOF Pro (Bruker) equipped with a CaptiveSpray source. Peptides (250 ng) were first injected onto a trap column (Acclaim PepMap 100 C18, 5mm X 300 µm, 5 µm particles; Thermo-Fisher, Germany) and next separated on a 25cm X 75µm analytical column, 1.6µm C18 beads with a packed emitter tip (Aurora Series with CSI, IonOpticks, Australia). The column temperature was maintained at 50°C using an integrated column oven. The column was equilibrated using 5 column volumes before loading sample in 100% buffer A (97.9% LC-MS grade water, 2% ACN, 0.1% FA). Samples were separated at 400nl/min using a linear gradient from 2% to 25% buffer B (99.9% ACN, 0.1% FA) over 90min before ramping to 37% (10min), and 95% of buffer B (10min) and sustained for 10min (total

separation method time 120min). The timsTOF Pro (Bruker) was operated in positive ion data dependent acquisition PASEF mode using Compass Hystar 5.1.8.1. Settings as follows: Mass Range 100 to 1700m/z, 1/K0 Start 0.6 V.s/cm^2 End 1.6 V./cm^2, Ramp time 100ms, Lock Duty Cycle to 100%, Capillary Voltage 1500V, Dry Gas 3 l/min, Dry Temp 180°C, PASEF settings: 10 MS/MS scans (total cycle time 1.16sec), charge range 0-5, active exclusion for 0.4 min, Scheduling Target intensity 20000, Intensity threshold 2500, variable CID collision energy 20-59 eV.

Raw data processing and analysis. Raw MS data were processed with the MaxQuant software package, version 1.6.17 using the built-in Andromeda search engine and the label-free quantitation algorithm as described previously[47]. Additionally, the intensity-based absolute quantification (iBAQ) algorithm and Match Between Runs option were used. Data were searched against the *Mesocricetus auratus* proteome (UniprotKB, release 2020_06) containing forward and reverse (decoy) sequences concatenated with the SARS-CoV-2 polyprotein with the individual viral open reading frames annotated manually. In MaxQuant, carbamidomethylation was set as fixed and methionine oxidation and N-acetylation as variable modifications. Search peptide tolerance was set at 70ppm and main search set at 30ppm (other settings left as default). Experiment type was set as TIMS-DDA with no modification to default settings. Search results were filtered with a false discovery rate (FDR) of 0.01 for peptide and protein identifications. The Perseus software package, version 1.6.10.4 was used to further process the data. Protein tables were filtered to eliminate the identifications from the reverse decoy database and common contaminants. In analyzing MS data, only proteins identified on the basis of at least one peptide and a minimum of three quantitation events in at least one experimental group were considered. IBAQ protein intensity values were normalized against the median intensity of each sample (using only peptides with recorded intensity values across all samples and biological replicas), log-transformed and missing values filled by imputation with random numbers drawn from a normal distribution calculated for each sample. Significantly regulated proteins were determined by multiple equal variance *t*-tests with permutation-based false discovery rate statistics. We performed 250 permutations and the FDR threshold was set at 0.05. The parameter S0 was set at 0.1 to separate background from specifically enriched interactors. Results were plotted as Volcano plot and heat map using the Perseus software package [48].

Data availability

The mass-spectrometry-based proteomics will be uploaded in public repositories. Unique dataset identifiers are pending.

Data analysis

All data were analyzed with the Prism software (GraphPad, 8.4.3) using Kruskal-Wallis one-way analysis of variance (ANOVA) followed by Dunn's multiple comparisons test or unpaired two-tailed Student's *t*-test as indicated in the respective legends. Statistical significance was defined as $p < 0.05$ ($*p < 0.05$, $**p < 0.01$, $***p < 0.001$). Additionally, ELISA data were evaluated using the "Four Parameter Logistic Curve" online data analysis tool, MyAssays Ltd., 25 th October 2012, http://www.myassays.com/four-parameter-logistic-curve.assay. Detection of outliers were performed using Grubbs' test in GraphPad QuickCalcs Outlier Calculator.

Author contributions

GG designed the study and wrote the manuscript. SSB and BS performed all animal experiments, analyzed the data and revised the manuscript. NMK, SB, MZ, TB, HJ, ZM, VPdR and VKB assisted with the animal experiments and performed molecular analysis. GB, KB and WB performed histopathological analysis of the animal organs. AK, CU and PS performed proteomic experiments and analysis. MS, DJ, AN and SK provided clinical samples from Covid-19 patients for SARS-CoV-2 virus isolation. KK analyzed the lungs of fatal Covid-19 cases. All authors approved the manuscript. We thank Martin Müller for technical assistance. We thank staff of the Core Facility Small Animal Models of the Heinrich Pette Institute, Leibniz Institute of Experimental Virology, particularly Ursula Müller and Oliver Strauch for their excellent support with the golden hamster model.

Acknowledgment

This study was supported by a rapid response grant from the federal ministry of health (BMG) to G.G. Further support was provided by a BMBF (Federal Ministry of Education and Research) project entitled RAPID (Risk assessment in re-pandemic respiratory infectious diseases), 01KI1723G and by the Ministry of Science and Culture of Lower Saxony in Germany (14 - 76103-184 CORONA-15/20) to W.B.. KK receives funding of the Ministry of Science, Research and the Arts Baden-Württemberg and the Deutsche Herzstiftung for research on SARS-CoV-2. AK acknowledges funding through Alexander von Humboldt foundation through a postdoctoral fellowship. AK and CU are furthermore supported through a rapid response grant from the federal ministry of health (BMG) and MS SPIDOC within the European Union's Horizon 2020 research and innovation program under grant agreement No. 801406.

Competing interest statement

The authors declare no competing interests.

Figure legends

Figure 1. SARS-CoV-2 pathogenesis in male and female golden hamsters. a, **b**, Weight loss of male (**a**) and female (**b**) golden hamsters infected with SARS-CoV-2 (10^5 p.f.u. ml^{-1}; male, *n* = 9; female *n* = 10), Poly(I:C) (*n* = 9) or PBS (*n* = 10). Statistical significance was assessed by Kruskal-Wallis one-way ANOVA (*p < 0.05, **p<0.01, ***p<0.001). **c**, Area under the curve (AUC) for body weight of SARS-CoV-2 infected male and female golden hamsters. **d**, Viral lung titers of SARS-CoV-2 infected golden hamsters (3d p.i., *n* = 5). **e**, Haematoxylin and eosin (HE) and SARS-CoV-2 nucleoprotein (NP) staining in lungs of infected golden hamsters (3 dpi; representative pictures are shown, *n* = 5). **f**, Viral plasma titers of SARS-CoV-2 infected golden hamsters (3d p.i., *n* = 5). **g**, **h**, Viral titers (**g**) and viral RNA levels (**h**) in testis of male golden hamsters (3d p.i., *n* = 5). **i**, HE staining of testis from male golden hamsters (3d p.i., *n* = 5). **j**, **k**, Viral titers (**j**) and viral RNA levels (**k**) in ovary of female golden hamsters (3d p.i., *n* = 5). **l**, HE staining of ovary from female golden hamsters (3d p.i., *n* = 5). **m**, **n**, Viral titers (**m**) and viral RNA levels (**n**) in uteri of female golden hamsters (3d p.i., *n* = 5). **o**, HE staining in uteri of female Syrian golden hamsters (3d p.i., *n* = 5). **a-d**,**f**,**g**,**h**,**j**,**k**,**m**,**n**, Values are shown as means, error bars as SD.

Figure 2. Immune response in the lungs of SARS-CoV-2 infected male and female golden hamsters. a, IL-6 mRNA expression levels (*n* = 5; male Poly(I:C): *n* = 4). **b**, IL-1ra mRNA expression levels (*n* = 5; male Poly(I:C): *n* = 4). **c**, **d**, Eotaxin mRNA (**c**) and protein (**d**) expression levels (*n* = 5; male Poly(I:C): *n* = 4). **e**, MIP-1α protein expression levels (*n* = 5). **f**, IFN-γ mRNA expression levels (*n* = 5; male Poly(I:C): *n* = 4). **g**, VEGF protein expression levels (*n* = 4; SARS-CoV-2: *n* = 3). **h**, IL-10 protein expression levels (*n* = 5). **i**, IL-12 protein expression levels (*n* = 5). **j**, IL-1β protein expression levels (*n* = 5). **k**, IL-2 protein expression levels (*n* = 5). **l**, IL-13 protein expression levels (*n* = 5). **m**, MIP-1b protein expression levels (*n* = 5). **n**, MCP-1 protein expression levels (*n* = 5). **o**, TNF-α protein expression levels (*n* = 5). Cytokine and chemokine levels were measured in lung homogenates at 3 d p.i.. Values are shown as means; error bars as SD; detection limits are indicated as dotted lines. Statistical significance was assessed by Kruskal-Wallis one-way ANOVA and by unpaired Student's *t*-test (*p < 0.05, **p<0.01).

Figure 3. Sex hormones and SARS-CoV-2 entry receptors in infected male and female golden hamsters. a, **b**, Testosterone levels in plasma of male (**a**) and female (**b**) golden

hamsters. **c**, **d**, Estradiol levels in plasma of male (**c**) and female (**d**) golden hamsters. **e**, **f**, Cortisol levels in plasma of male (**e**) and female (**f**) golden hamsters. **g**, **h**, Progesterone levels in plasma of male (**g**) and female (**h**) golden hamsters. Values are shown as means; error bars are shown as SD (n = 5; estradiol male3d p.i.: n = 10; estradiol male 14d p.i. SARS-CoV-2: n = 4; estradiol female 3d p.i. Poly(I:C) and SARS-CoV-2: each n = 8). **i-k**, ACE2 mRNA expression levels at day 1 (**i**), 3 (**j**) and 6 (**k**) p.i. (n = 5; male Poly(I:C) 1d p.i.: n = 4; male and female Poly(I:C) 3d p.i.: n = 4) in the lungs of infected golden hamsters. **l,** ACE mRNA expression levels (n = 5; male Poly(I:C): n = 4) in the lungs of infected golden hamsters. **m**, **n**, ACE2 mRNA expression levels in testis of male (**m**) and ovary of female (**n**) golden hamsters at day 3 p.i. (n = 5; male SARS-CoV-2: n = 4). **o,** DPP4 mRNA expression levels (n = 5; male Poly(I:C): n = 4) in the lungs of infected golden hamsters. **p**, **q**, TMPRSS2 mRNA expression levels at day 3 (**p**) and 6 (**q**) p.i. in the lungs of infected golden hamsters. **r**, AR mRNA expression levels in the lungs of infected golden hamsters (n = 5; Poly(I:C): n = 4). **s**, ZIP9 mRNA expression levels in the lungs of infected golden hamsters (n = 5; male Poly(I:C): n = 4). The mRNA expression levels are presented as negative exponents of Δ*ct* values; values are shown as means; error bars are shown as SD. Statistical significance was assessed by Kruskal-Wallis one-way ANOVA (*p < 0.05, **p < 0.01, ***p < 0.001).

Figure 4. Proteomic analysis of the lungs of SARS-CoV-2 infected male and female golden hamsters. a, Volcano plot displaying host proteins up- or down-regulated in male versus female golden hamsters upon SARS-CoV-2 infection (orange and green dots, respectively). Significantly-regulated proteins are separated from background proteins by a hyperbolic curve (dotted grey line). **b**, Heatmap of iBAQ intensities for significantly regulated proteins (Student's t-test, FDR 0.05, p < 0.05) in the total proteome across experimental groups and biological replicates.

Figure 5. CYP19A1 and endothelial activation in the lungs of SARS-CoV-2 infected male and female golden hamsters. a, Schematic overview of binding sites for transcription factors in the four promoter regions (P1, P2, P3, and P4) of the aromatase gene CYP19A1. **b-d**, Aromatase mRNA expression levels at day 1 (**b**), 3 (**c**) and 6 (**d**) p.i. (n = 5; male Poly(I:C): n = 4). **e**, 5α-Reductase mRNA expression levels (n = 5; male Poly(I:C): n = 4). **f**, **g**, Aromatase mRNA expression levels in testis of male (**f**) and ovary of female (**g**) golden hamsters at 3d p.i. (n = 5; male SARS-CoV-2: n = 4). **h**, **i**, Endothelial lipase mRNA expression levels at day 3 (**h**) and 6 (**i**) p.i. (n = 5; male Poly(I:C) 3d p.i.: n = 4). The mRNA expression levels are presented

as negative exponents of *ct* values; values are shown as means; error bars are shown as SD, detection limits are indicated as dotted lines. Statistical significance was assessed by Kruskal-Wallis one-way ANOVA (*p < 0.05, **p < 0.01).

Figure 6. CYP19A1 protein expression in the lungs of SARS-CoV-2 infected male and female golden hamsters. a, **b**, Immunohistochemistry of serial sections from lungs of male (**a**) and female (**b**) golden hamsters for aromatase, SARS-CoV-2 NP, macrophages (CD204), endothelial cells (vWF and CD31), T cells (CD3) and smooth muscle (SMA). Bronchus (B), vessel (V), alveola (A), stars indicate perivascular connective tissue and arrowheads indicate macrophages. Representative pictures are shown. **c**-**f** Semiquantitative scoring of the of aromatase CYP19A1 immunoreactivity in different lung regions of male and female golden hamsters at day 3 p.i. (n = 5). Immunoreactivitiy was examined by light microscopy in the endothelium (**c**), the bronchiolar epithelium (**d**), the perivascular (**e**) and peribronchiolar region (**f**) in the lungs of infected hamsters. Signal intensity in respective regions was very low (0,5), low (1), low to moderate (2), moderate (3), moderate to high (4), or high (5). Signal distribution was assessed as: focal/oligofocal (≤3 foci; 1), multifocal (>3 foci; 2) and diffuse (3). For better comparative interpretation a final score for each region and animal was calculated as product of signal intensity times signal distribution. Statistical significance was assessed by Kruskal-Wallis one-way ANOVA and by unpaired Student's *t*-test (*p < 0.05, **p<0.01).

Figure 7. CYP19A1 protein expression in the lungs of fatal Covid-19 cases. Immunohistochemistry of lungs from male (**a**-**d**) and female (**f**-**h**) patients with Covid-19 or controls (**e**; representative picture of n = 3 are shown) stained for aromatase. The intensity of staining was significantly higher in endothelial cells and especially in macrophages in male (**a**-**d**) compared to female (**f**-**h**) Covid-19 patients and control patients (**e**). Stars indicate endothelial cells and arrowheads indicate macrophages. Scale bar, 100 µm.

Extended Data Figure 1. Viral load in SARS-CoV-2 infected male and female golden hamsters. a, Viral lung titers of SARS-CoV-2 infected golden hamsters at 6d p.i. (n = 5). **b**, Haematoxylin and eosin (HE) and SARS-CoV-2 nucleoprotein (NP) staining in lungs of infected golden hamsters at 6d p.i. (representative pictures are shown, n = 5).

Extended Data Figure 2. Immune response in the lungs of SARS-CoV-2 infected male and female golden hamsters. a-**k**, Cytokine and chemokine expression levels at day 1 p.i. for

eotaxin (**a**), MIP-1α (**b**), IFN-γ (**c**), VEGF (**d**), IL-10 (**e**), IL-12 (**f**), IL-1β (**g**), IL-2 (**h**), IL-13 (**i**), MIP-1β (**j**) and TNF-α (**k**). **l-s**, Cytokine and chemokine expression levels at day 6 p.i. for eotaxin (**l**), MIP-1α (**m**), IFN-γ (**n**), VEGF (**o**), IL-12 (**p**), IL-2 (**q**), MIP-1β (**r**) and TNF-α (**s**). Cytokine and chemokine levels were measured in lung homogenisates (n = 5). Values are shown as means; error bars as SD; detection limits are indicated as dotted lines. Statistical significance was assessed by Kruskal-Wallis one-way ANOVA and by unpaired Student's t-test (*$p < 0.05$, **$p<0.01$).

Extended Data Figure 3. Immune response in the plasma of SARS-CoV-2 infected male and female golden hamsters. a-k, Cytokine and chemokine expression levels at day 1 p.i. for eotaxin (**a**), MIP-1α (**b**), IFN-γ (**c**), VEGF (**d**), IL-10 (**e**), IL-12 (**f**), IL-1β (**g**), IL-2 (**h**), IL-13 (**i**), MCP-1 (**j**) and TNF-α (**k**). **l-s**, Cytokine and chemokine expression levels at day 3 p.i. for eotaxin (**l**), MIP-1α (**m**), VEGF (**n**), IL-1β (**o**), IL-2 (**p**), IL-13 (**q**), MCP-1 (**r**) and TNF-α (**s**). **t-z2**, Cytokine and chemokine expression levels at day 6 p.i. for eotaxin (**t**), MIP-1α (**u**), IFN-γ (**v**), VEGF (**w**), IL-1β (**x**), IL-2 (**y**), MCP-1 (**z1**) and TNF-α (**z2**).Cytokine and chemokine levels were measured in plasma (n = 5). Values are shown as means; error bars as SD; detection limits are indicated as dotted lines. Statistical significance was assessed by Kruskal-Wallis one-way ANOVA and by unpaired Student's t-test (*$p < 0.05$).

Extended Data Figure 4. Testosterone and estradiol levels in influenza A virus infected male mice. a, **b**, Testosterone (**a**) and estradiol (**b**) levels in plasma of H7N9 influenza A virus infected male mice. **c**, **d**, Testosterone (**a**) and estradiol (**b**) levels in plasma of pH1N1 influenza A virus infected male mice. Values are shown as means; error bars are shown as SD (n = 5; testosterone pH1N1: n = 4). Statistical significance was assessed by unpaired Student's t-test (**$p < 0.01$).

Extended Data Figure 5. Proteomic profile in the lungs of SARS-CoV-2 infected male golden hamsters. Heatmap of iBAQ intensities for significantly regulated proteins in SARS-CoV-2 infected male golden hamsters compared to PBS control group (Student's t-test, FDR 0.05, $p < 0.05$) in the total proteome across experimental groups and biological replicates. Female and male animals are indicated in light pink and blue, respectively. Each column represent an individual hamster. Gray color represents missing values (not determined (ND)).

Extended Data Figure 6. Proteomic profile in the lungs of SARS-CoV-2 infected female golden hamsters. Heatmap of iBAQ intensities for significantly regulated proteins in SARS-CoV-2 infected male hamsters compared to PBS control group (Student's *t*-test, FDR 0.05, $p < 0.05$) in the total proteome across experimental groups and biological replicates. Female and male animals are indicated in light pink and blue, respectively. Each column represent an individual hamster. Gray color represents missing values (not determined (ND)).

Extended Data Figure 7. CYP19A1 protein expression in the lungs of SARS-CoV-2 infected male and female golden hamsters. a, **b**, Immunohistochemistry of serial sections from lungs of male (**a**) and female (**b**) golden hamsters for aromatase, SARS-CoV-2 NP, macrophages (CD204), endothelial cells (vWF and CD31), T cells (CD3) and smooth muscle (SMA). Inlets from these overview pictures are shown in Figure 6.

Extended Data Figure 8. Hormone levels in the gonads of SARS-CoV-2 infected male and female golden hamsters.

a, **b**, Testosterone levels in testis of male (**a**) and ovary of female (**b**) golden hamsters. **c**, **d**, Estradiol levels in testis of male (**c**) and ovary of female (**d**) golden hamsters. **e**, **f**, Cortisol levels in testis of male (**e**) and ovary of female (**f**) golden hamsters. **g**, **h**, Progesterone levels in testis of male (**g**) and ovary of female (**h**) golden hamsters. Values are shown as means; error bars are shown as SD ($n = 5$; male SARS-CoV-2 14d p.i.: $n = 4$; estradiol female PBS and Poly(I:C): each $n = 4$). Statistical significance was assessed by Kruskal-Wallis one-way ANOVA (*$p < 0.05$, **$p < 0.01$).

Extended Data Figure 9. Model of CYP19A mediated lung pathology in SARS-CoV-2 infection. We propose that the lung plays a key role in the aromatization of testosterone-to-estradiol. Since CYP19A1 is expressed to higher levels in males than females, the conversion of testosterone-to-estradiol is enhanced in males. Elevated estradiol levels may fulfill their endocrine and paracrine functions. Since most immune cells, e.g. macrophages possess androgen and estrogen receptors their activation will be dependent on the availability of the respective sex hormone. Particularly estradiol plays an important role in endothelial inflammation. Thus, males might be more prone to CYP19A1 driven endothelial inflammation.

References

1 5050., G. H. Sex-Disaggregated Data Tracker. https://globalhealth5050.org/the-sex-gender-and-covid-19-project (2020).

2 Williamson, E. J. *et al.* Factors associated with COVID-19-related death using OpenSAFELY. *Nature* **584**, 430-436, doi:10.1038/s41586-020-2521-4 (2020).

3 Clark, A. *et al.* Global, regional, and national estimates of the population at increased risk of severe COVID-19 due to underlying health conditions in 2020: a modelling study. *Lancet Glob Health* **8**, e1003-e1017, doi:10.1016/S2214-109X(20)30264-3 (2020).

4 Jin, J. M. *et al.* Gender Differences in Patients With COVID-19: Focus on Severity and Mortality. *Front Public Health* **8**, 152, doi:10.3389/fpubh.2020.00152 (2020).

5 Krieger, N., Chen, J. T. & Waterman, P. D. Excess mortality in men and women in Massachusetts during the COVID-19 pandemic. *Lancet* **395**, 1829, doi:10.1016/S0140-6736(20)31234-4 (2020).

6 Gebhard, C., Regitz-Zagrosek, V., Neuhauser, H. K., Morgan, R. & Klein, S. L. Impact of sex and gender on COVID-19 outcomes in Europe. *Biol Sex Differ* **11**, 29, doi:10.1186/s13293-020-00304-9 (2020).

7 Bhopal, S. S. & Bhopal, R. Sex differential in COVID-19 mortality varies markedly by age. *Lancet* **396**, 532-533, doi:10.1016/S0140-6736(20)31748-7 (2020).

8 Haitao, T. *et al.* COVID-19 and Sex Differences: Mechanisms and Biomarkers. *Mayo Clin Proc* **95**, 2189-2203, doi:10.1016/j.mayocp.2020.07.024 (2020).

9 Imai, M. *et al.* Syrian hamsters as a small animal model for SARS-CoV-2 infection and countermeasure development. *Proc Natl Acad Sci U S A* **117**, 16587-16595, doi:10.1073/pnas.2009799117 (2020).

10 Sia, S. F. *et al.* Pathogenesis and transmission of SARS-CoV-2 in golden hamsters. *Nature* **583**, 834-838, doi:10.1038/s41586-020-2342-5 (2020).

11 Kadel, S. & Kovats, S. Sex Hormones Regulate Innate Immune Cells and Promote Sex Differences in Respiratory Virus Infection. *Front Immunol* **9**, 1653, doi:10.3389/fimmu.2018.01653 (2018).

12 Tuku, B. *et al.* Testosterone Protects Against Severe Influenza by Reducing the Pro-Inflammatory Cytokine Response in the Murine Lung. *Front Immunol* **11**, 697, doi:10.3389/fimmu.2020.00697 (2020).

13 Lin, B. *et al.* Prostate-localized and androgen-regulated expression of the membrane-bound serine protease TMPRSS2. *Cancer Res* **59**, 4180-4184 (1999).

14 Mjaess, G., Karam, A., Aoun, F., Albisinni, S. & Roumeguere, T. COVID-19 and the male susceptibility: the role of ACE2, TMPRSS2 and the androgen receptor. *Prog Urol* **30**, 484-487, doi:10.1016/j.purol.2020.05.007 (2020).

15 Glowacka, I. *et al.* Differential downregulation of ACE2 by the spike proteins of severe acute respiratory syndrome coronavirus and human coronavirus NL63. *J Virol* **84**, 1198-1205, doi:10.1128/JVI.01248-09 (2010).

16 Kuba, K. *et al.* A crucial role of angiotensin converting enzyme 2 (ACE2) in SARS coronavirus-induced lung injury. *Nat Med* **11**, 875-879, doi:10.1038/nm1267 (2005).

17 Sajuthi, S. P. *et al.* Type 2 and interferon inflammation regulate SARS-CoV-2 entry factor expression in the airway epithelium. *Nat Commun* **11**, 5139, doi:10.1038/s41467-020-18781-2 (2020).

18 Targonska-Stepniak, B. & Majdan, M. Serum amyloid A as a marker of persistent inflammation and an indicator of cardiovascular and renal involvement in patients with rheumatoid arthritis. *Mediators Inflamm* **2014**, 793628, doi:10.1155/2014/793628 (2014).

19 Nathan, L. *et al.* Testosterone inhibits early atherogenesis by conversion to estradiol: critical role of aromatase. *Proc Natl Acad Sci U S A* **98**, 3589-3593, doi:10.1073/pnas.051003698 (2001).

20 Harada, N. *et al.* Localized expression of aromatase in human vascular tissues. *Circ Res* **84**, 1285-1291, doi:10.1161/01.res.84.11.1285 (1999).

21 Diano, S. *et al.* Aromatase and estrogen receptor immunoreactivity in the coronary arteries of monkeys and human subjects. *Menopause* **6**, 21-28 (1999).

22 Nebert, D. W., Wikvall, K. & Miller, W. L. Human cytochromes P450 in health and disease. *Philos Trans R Soc Lond B Biol Sci* **368**, 20120431, doi:10.1098/rstb.2012.0431 (2013).

23 Enjuanes, A. *et al.* Functional analysis of the I.3, I.6, pII and I.4 promoters of CYP19 (aromatase) gene in human osteoblasts and their role in vitamin D and dexamethasone stimulation. *Eur J Endocrinol* **153**, 981-988, doi:10.1530/eje.1.02032 (2005).

24 Kamat, A., Graves, K. H., Smith, M. E., Richardson, J. A. & Mendelson, C. R. A 500-bp region, approximately 40 kb upstream of the human CYP19 (aromatase) gene, mediates placenta-specific expression in transgenic mice. *Proc Natl Acad Sci U S A* **96**, 4575-4580, doi:10.1073/pnas.96.8.4575 (1999).

25 Sebastian, S., Takayama, K., Shozu, M. & Bulun, S. E. Cloning and characterization of a novel endothelial promoter of the human CYP19 (aromatase P450) gene that is up-regulated in breast cancer tissue. *Mol Endocrinol* **16**, 2243-2254, doi:10.1210/me.2002-0123 (2002).

26 Toda, K. *et al.* Structural and functional characterization of human aromatase P-450 gene. *Eur J Biochem* **193**, 559-565, doi:10.1111/j.1432-1033.1990.tb19372.x (1990).

27 Zhao, Y., Mendelson, C. R. & Simpson, E. R. Characterization of the sequences of the human CYP19 (aromatase) gene that mediate regulation by glucocorticoids in adipose stromal cells and fetal hepatocytes. *Mol Endocrinol* **9**, 340-349, doi:10.1210/mend.9.3.7776980 (1995).

28 Badellino, K. O., Wolfe, M. L., Reilly, M. P. & Rader, D. J. Endothelial lipase concentrations are increased in metabolic syndrome and associated with coronary atherosclerosis. *PLoS Med* **3**, e22, doi:10.1371/journal.pmed.0030022 (2006).

29 Lamarche, B. & Paradis, M. E. Endothelial lipase and the metabolic syndrome. *Curr Opin Lipidol* **18**, 298-303, doi:10.1097/MOL.0b013e328133857f (2007).

30 Chen, Y. *et al.* Low testosterone levels in H7N9 infected men correlate with high cytokine responses and lethal outcome: a retrospective cohort study. *medRxiv* (2020).

31 Schroeder, M. *et al.* The majority of male patients with COVID-19 present low testosterone levels on admission to Intensive Care in Hamburg, Germany: a retrospective cohort study. *medRxiv* **https://doi.org/10.1101/2020.05.07.20073817** (2020).

32 Ding, T. *et al.* Potential Influence of Menstrual Status and Sex Hormones on female SARS-CoV-2 Infection: A Cross-sectional Study from Multicentre in Wuhan, China. *Clin Infect Dis*, doi:10.1093/cid/ciaa1022 (2020).

33 Biegon, A. In vivo visualization of aromatase in animals and humans. *Front Neuroendocrinol* **40**, 42-51, doi:10.1016/j.yfrne.2015.10.001 (2016).

34 Wichmann, D. *et al.* Autopsy Findings and Venous Thromboembolism in Patients With COVID-19: A Prospective Cohort Study. *Ann Intern Med* **173**, 268-277, doi:10.7326/M20-2003 (2020).

35 Perico, L. *et al.* Immunity, endothelial injury and complement-induced coagulopathy in COVID-19. *Nat Rev Nephrol*, doi:10.1038/s41581-020-00357-4 (2020).

36 Mor, G. *et al.* Macrophages, estrogen and the microenvironment of breast cancer. *J Steroid Biochem Mol Biol* **67**, 403-411, doi:10.1016/s0960-0760(98)00143-5 (1998).

37 Becerra-Diaz, M., Song, M. & Heller, N. Androgen and Androgen Receptors as Regulators of Monocyte and Macrophage Biology in the Healthy and Diseased Lung. *Front Immunol* **11**, 1698, doi:10.3389/fimmu.2020.01698 (2020).

38 Artigalas, O., Vanni, T., Hutz, M. H., Ashton-Prolla, P. & Schwartz, I. V. Influence of CYP19A1 polymorphisms on the treatment of breast cancer with aromatase inhibitors: a systematic review and meta-analysis. *BMC Med* **13**, 139, doi:10.1186/s12916-015-0373-9 (2015).

39 Han, W. *et al.* Role of myeloid cell CYP19A1 in lung airway tissue repair following naphtalane induced epithelial injury in a mouse mode. *The FASEB Journal* **34** (2020).

40 D'Alessio, F. R. & Heller, N. M. COVID-19 and myeloid cells: complex interplay correlates with lung severity. *J Clin Invest*, doi:10.1172/JCI143361 (2020).

41 Merad, M. & Martin, J. C. Pathological inflammation in patients with COVID-19: a key role for monocytes and macrophages. *Nat Rev Immunol* **20**, 355-362, doi:10.1038/s41577-020-0331-4 (2020).
42 Corona, G. *et al.* Hypogonadism as a risk factor for cardiovascular mortality in men: a meta-analytic study. *Eur J Endocrinol* **165**, 687-701, doi:10.1530/EJE-11-0447 (2011).
43 Fernandez, C. J., Chacko, E. C. & Pappachan, J. M. Male Obesity-related Secondary Hypogonadism - Pathophysiology, Clinical Implications and Management. *Eur Endocrinol* **15**, 83-90, doi:10.17925/EE.2019.15.2.83 (2019).
44 Mushannen, T., Cortez, P., Stanford, F. C. & Singhal, V. Obesity and Hypogonadism-A Narrative Review Highlighting the Need for High-Quality Data in Adolescents. *Children (Basel)* **6**, doi:10.3390/children6050063 (2019).
45 Dandona, P. & Dhindsa, S. Update: Hypogonadotropic hypogonadism in type 2 diabetes and obesity. *J Clin Endocrinol Metab* **96**, 2643-2651, doi:10.1210/jc.2010-2724 (2011).
46 Bosmuller, H. *et al.* The evolution of pulmonary pathology in fatal COVID-19 disease: an autopsy study with clinical correlation. *Virchows Arch* **477**, 349-357, doi:10.1007/s00428-020-02881-x (2020).
47 Tyanova, S., Temu, T. & Cox, J. The MaxQuant computational platform for mass spectrometry-based shotgun proteomics. *Nat Protoc* **11**, 2301-2319, doi:10.1038/nprot.2016.136 (2016).
48 Tyanova, S. *et al.* The Perseus computational platform for comprehensive analysis of (prote)omics data. *Nat Methods* **13**, 731-740, doi:10.1038/nmeth.3901 (2016).

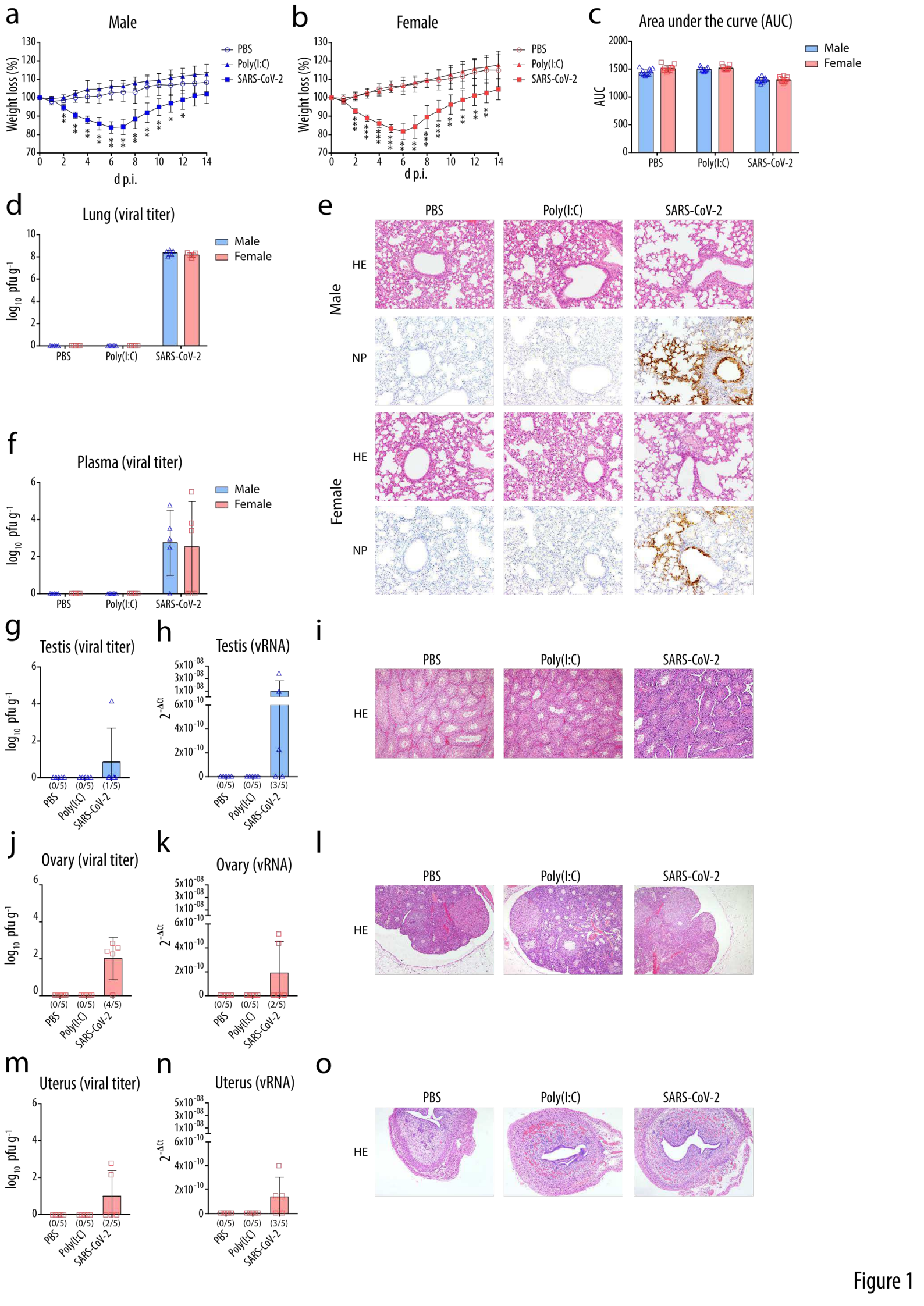
a
Male
Weight loss (%)
d p.i.
PBS
Poly(I:C)
SARS-CoV-2
b
Female
c
Area under the curve (AUC)
AUC
Male
Female
d
Lung (viral titer)
log10 pfu g-1
e
PBS
Poly(I:C)
SARS-CoV-2
HE
NP
Male
Female
f
Plasma (viral titer)
g
Testis (viral titer)
h
Testis (vRNA)
2-ΔCt
(0/5)
(1/5)
(3/5)
i
j
Ovary (viral titer)
(4/5)
k
Ovary (vRNA)
(2/5)
l
m
Uterus (viral titer)
n
Uterus (vRNA)
o

Figure 1

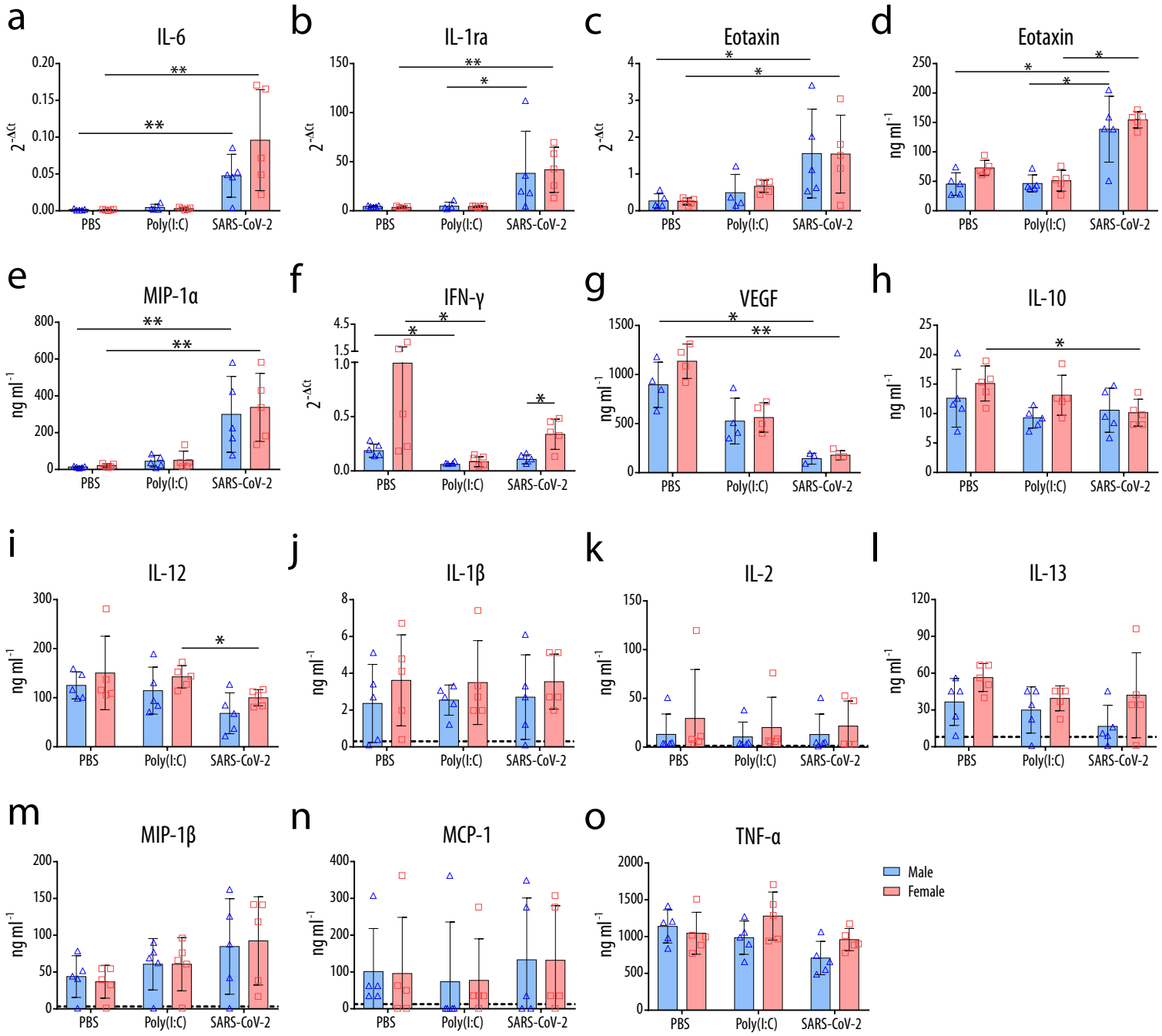
a
IL-6
b
IL-1ra
c
Eotaxin
d
Eotaxin
e
MIP-1α
f
IFN-γ
g
VEGF
h
IL-10
i
IL-12
j
IL-1β
k
IL-2
l
IL-13
m
MIP-1β
n
MCP-1
o
TNF-α
PBS
Poly(I:C)
SARS-CoV-2
Male
Female

Figure 2

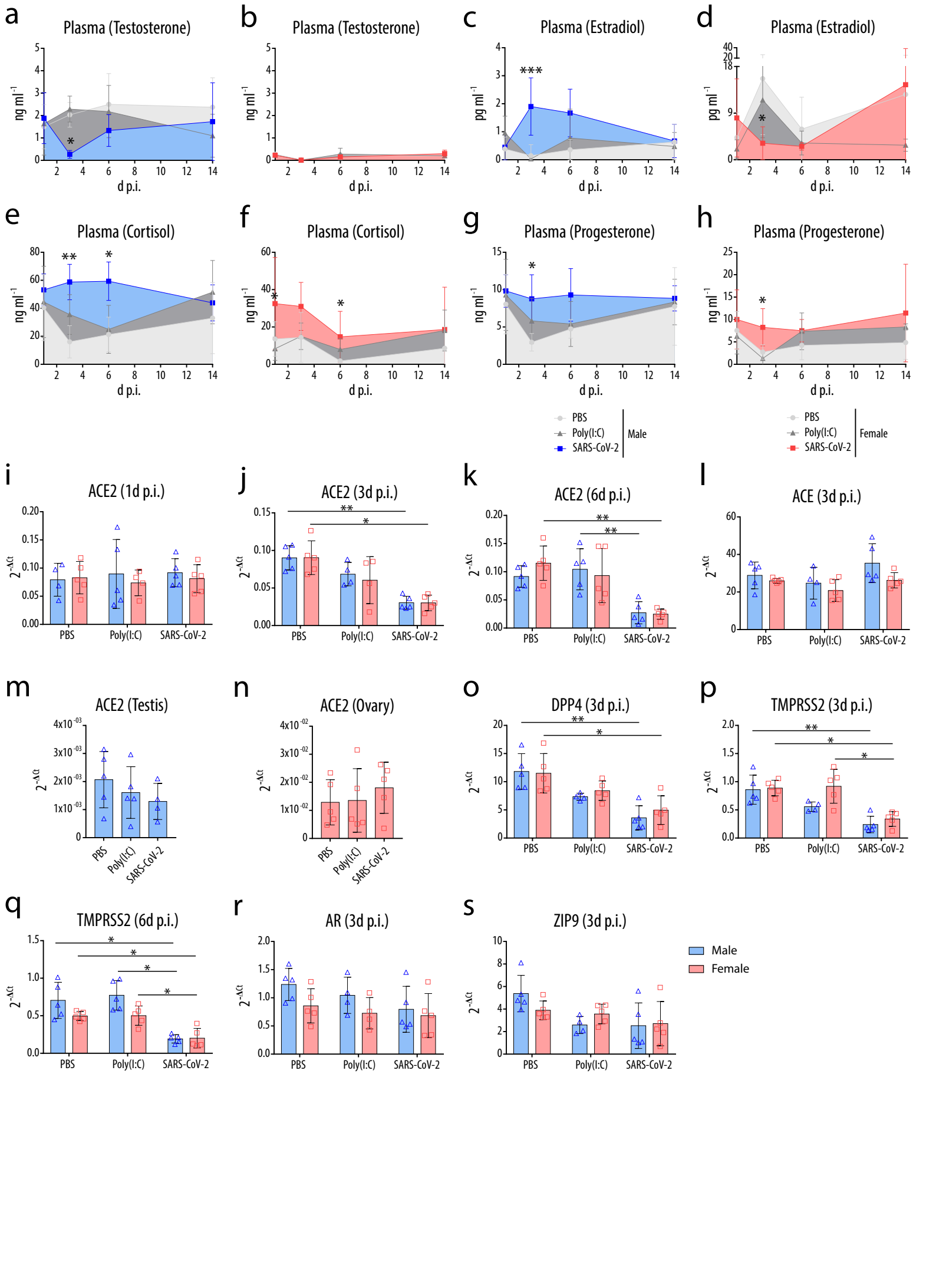
a
Plasma (Testosterone)
ng ml-1
d p.i.
b
Plasma (Testosterone)
ng ml-1
d p.i.
c
Plasma (Estradiol)
pg ml-1
d p.i.
d
Plasma (Estradiol)
pg ml-1
d p.i.
e
Plasma (Cortisol)
ng ml-1
d p.i.
f
Plasma (Cortisol)
ng ml-1
d p.i.
g
Plasma (Progesterone)
ng ml-1
d p.i.
h
Plasma (Progesterone)
ng ml-1
d p.i.
PBS
Poly(I:C)
SARS-CoV-2
Male
PBS
Poly(I:C)
SARS-CoV-2
Female
i
ACE2 (1d p.i.)
2-ΔCt
PBS
Poly(I:C)
SARS-CoV-2
j
ACE2 (3d p.i.)
2-ΔCt
PBS
Poly(I:C)
SARS-CoV-2
k
ACE2 (6d p.i.)
2-ΔCt
PBS
Poly(I:C)
SARS-CoV-2
l
ACE (3d p.i.)
2-ΔCt
PBS
Poly(I:C)
SARS-CoV-2
m
ACE2 (Testis)
2-ΔCt
PBS
Poly(I:C)
SARS-CoV-2
n
ACE2 (Ovary)
2-ΔCt
PBS
Poly(I:C)
SARS-CoV-2
o
DPP4 (3d p.i.)
2-ΔCt
PBS
Poly(I:C)
SARS-CoV-2
p
TMPRSS2 (3d p.i.)
2-ΔCt
PBS
Poly(I:C)
SARS-CoV-2
q
TMPRSS2 (6d p.i.)
2-ΔCt
PBS
Poly(I:C)
SARS-CoV-2
r
AR (3d p.i.)
2-ΔCt
PBS
Poly(I:C)
SARS-CoV-2
s
ZIP9 (3d p.i.)
2-ΔCt
PBS
Poly(I:C)
SARS-CoV-2
Male
Female

Figure 3

a

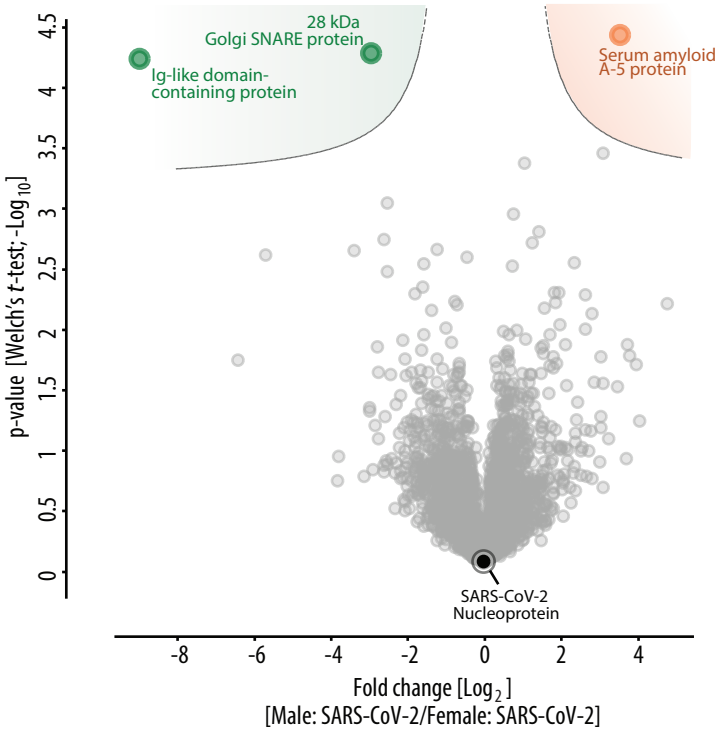
28 kDa
Golgi SNARE protein
Ig-like domain-
containing protein
Serum amyloid
A-5 protein
SARS-CoV-2
Nucleoprotein
p-value [Welch's t-test; -Log10]
0
0.5
1
1.5
2
2.5
3
3.5
4
4.5
-8
-6
-4
-2
0
2
4
Fold change [Log2]
[Male: SARS-CoV-2/Female: SARS-CoV-2]

b

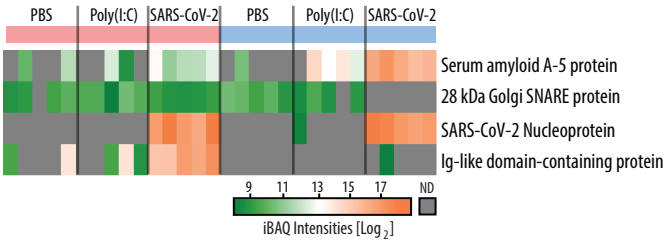
PBS
Poly(I:C)
SARS-CoV-2
PBS
Poly(I:C)
SARS-CoV-2
Serum amyloid A-5 protein
28 kDa Golgi SNARE protein
SARS-CoV-2 Nucleoprotein
Ig-like domain-containing protein
9
11
13
15
17
ND
iBAQ Intensities [Log2]

Figure 4

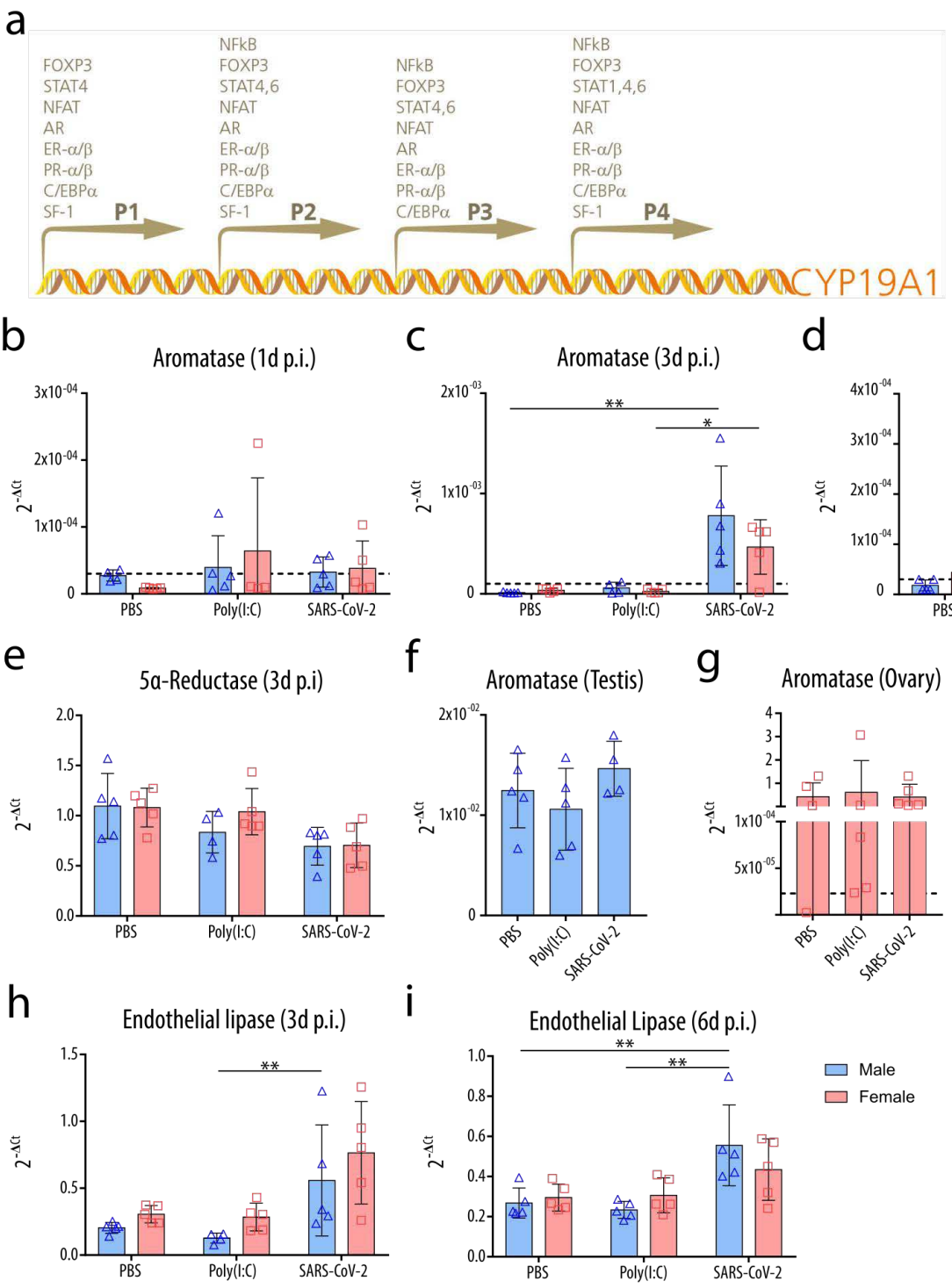
a
FOXP3
STAT4
NFAT
AR
ER-α/β
PR-α/β
C/EBPα
SF-1
P1
NFkB
FOXP3
STAT4,6
NFAT
AR
ER-α/β
PR-α/β
C/EBPα
SF-1
P2
NFkB
FOXP3
STAT4,6
NFAT
AR
ER-α/β
PR-α/β
C/EBPα
P3
NFkB
FOXP3
STAT1,4,6
NFAT
AR
ER-α/β
PR-α/β
C/EBPα
SF-1
P4
CYP19A1
b
Aromatase (1d p.i.)
c
Aromatase (3d p.i.)
d
Aromatase (6d p.i.)
e
5α-Reductase (3d p.i)
f
Aromatase (Testis)
g
Aromatase (Ovary)
h
Endothelial lipase (3d p.i.)
i
Endothelial Lipase (6d p.i.)
PBS
Poly(I:C)
SARS-CoV-2
Male
Female

Figure 5

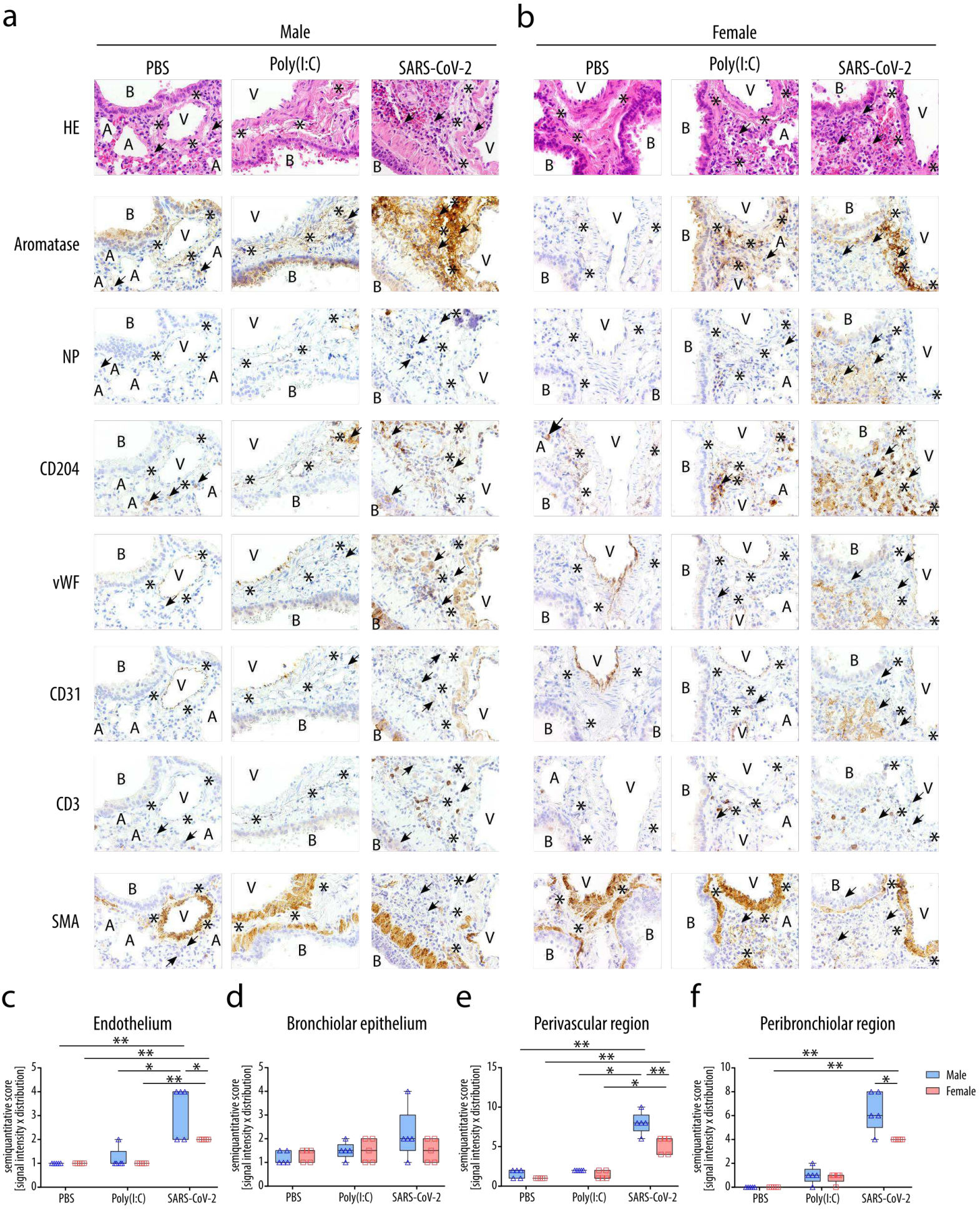
a
Male
PBS
Poly(I:C)
SARS-CoV-2
b
Female
PBS
Poly(I:C)
SARS-CoV-2
HE
Aromatase
NP
CD204
vWF
CD31
CD3
SMA
B
V
A
c
Endothelium
d
Bronchiolar epithelium
e
Perivascular region
f
Peribronchiolar region
semiquantitative score
[signal intensity x distribution]
PBS
Poly(I:C)
SARS-CoV-2
Male
Female

Figure 6

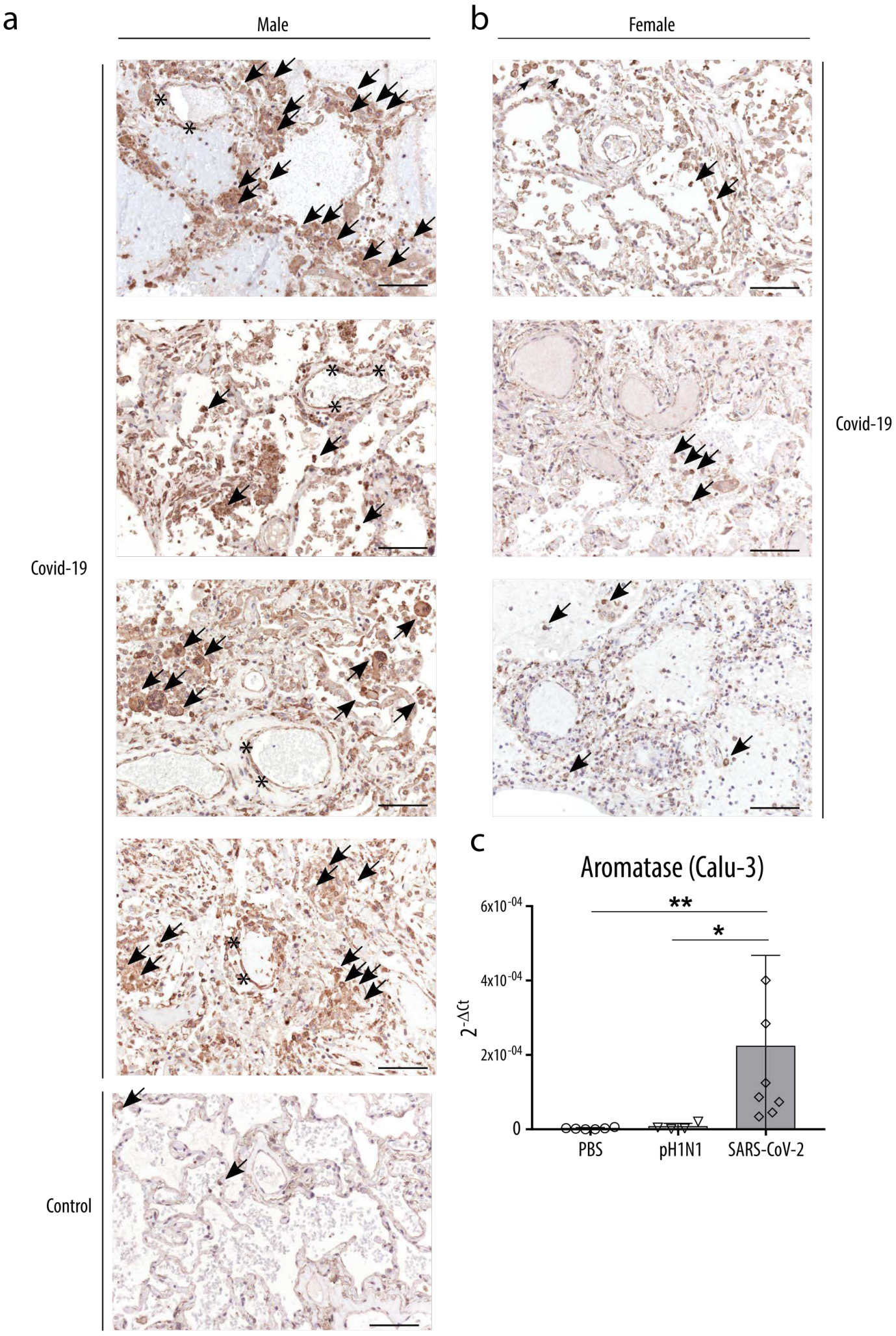
a
Male
b
Female
Covid-19
Covid-19
Control
c
Aromatase (Calu-3)
6x10-04
4x10-04
2x10-04
0
2-ΔCt
**
*
PBS
pH1N1
SARS-CoV-2

Figure 7

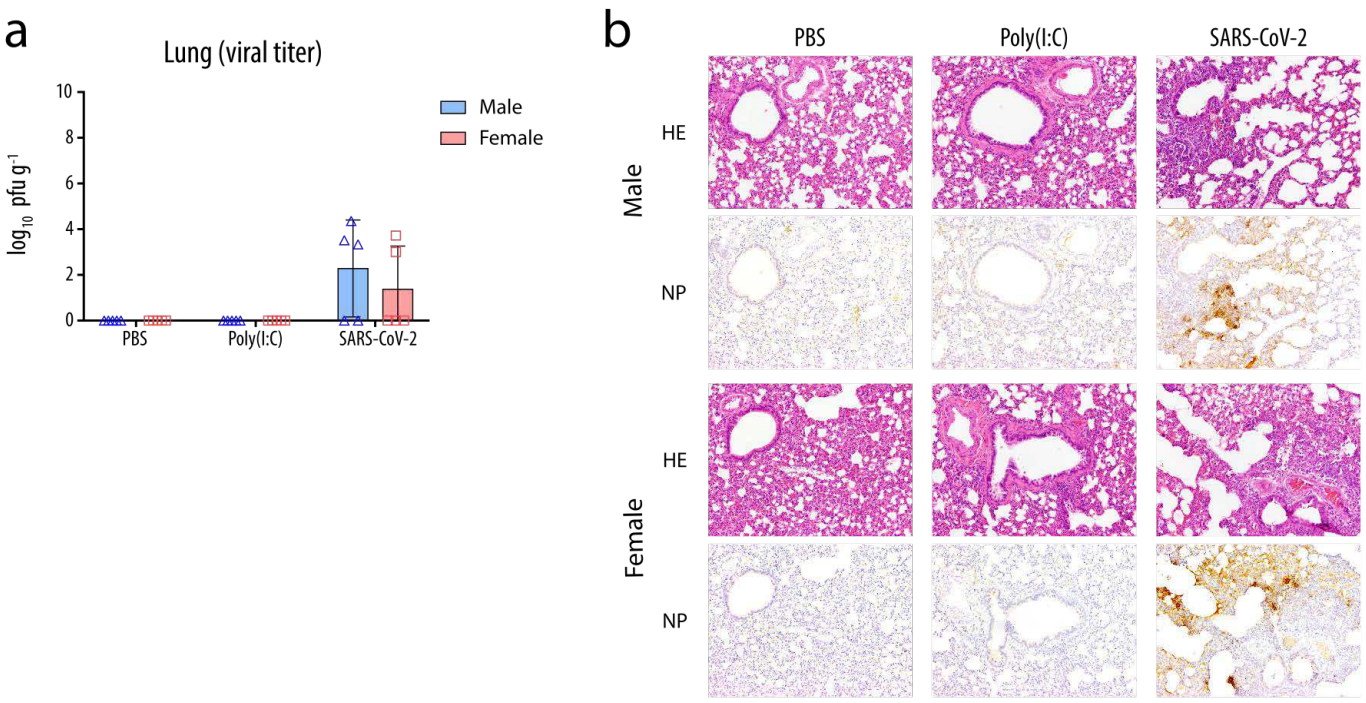

Extended Data Figure 1

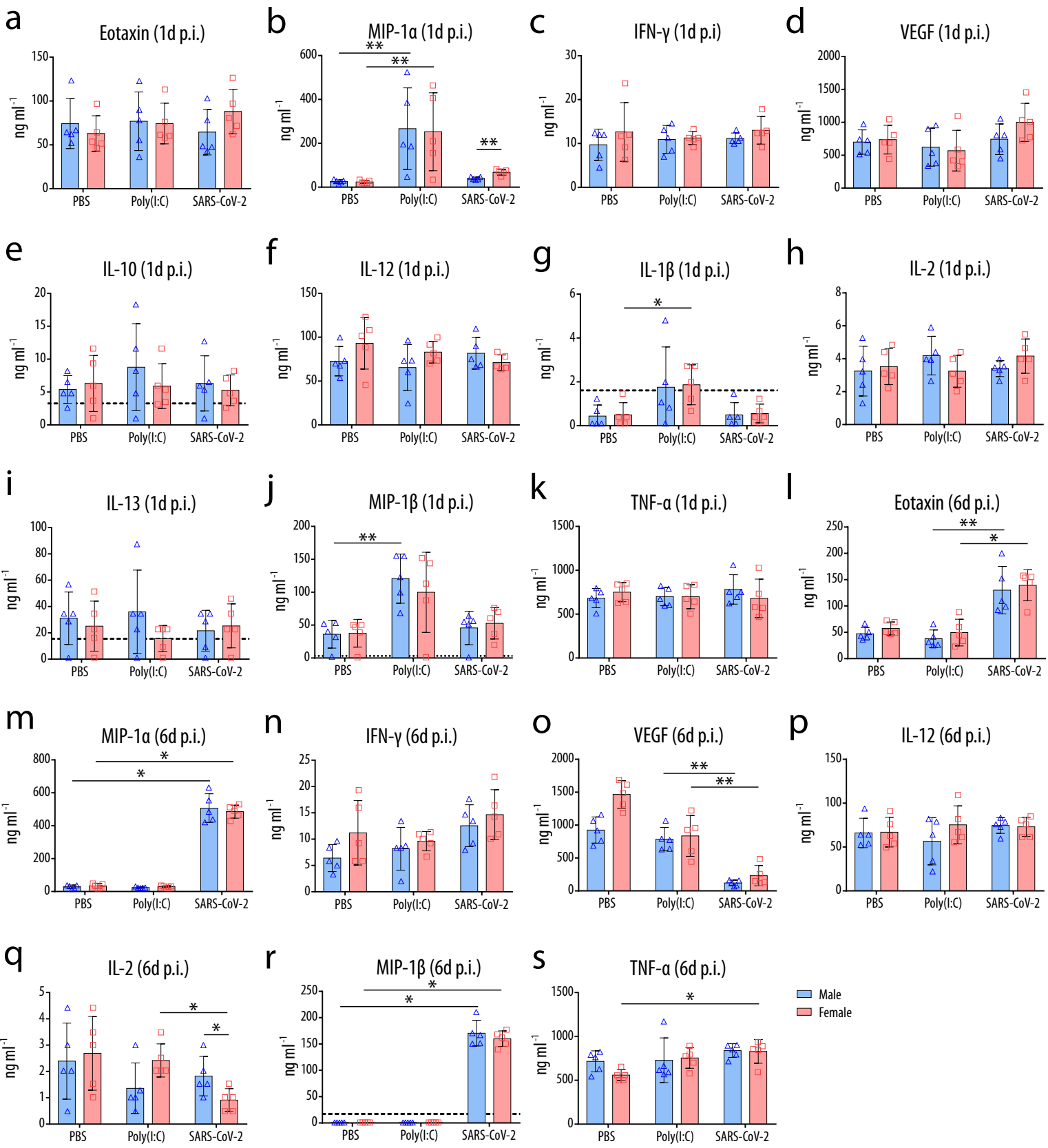

Extended Data Figure 2

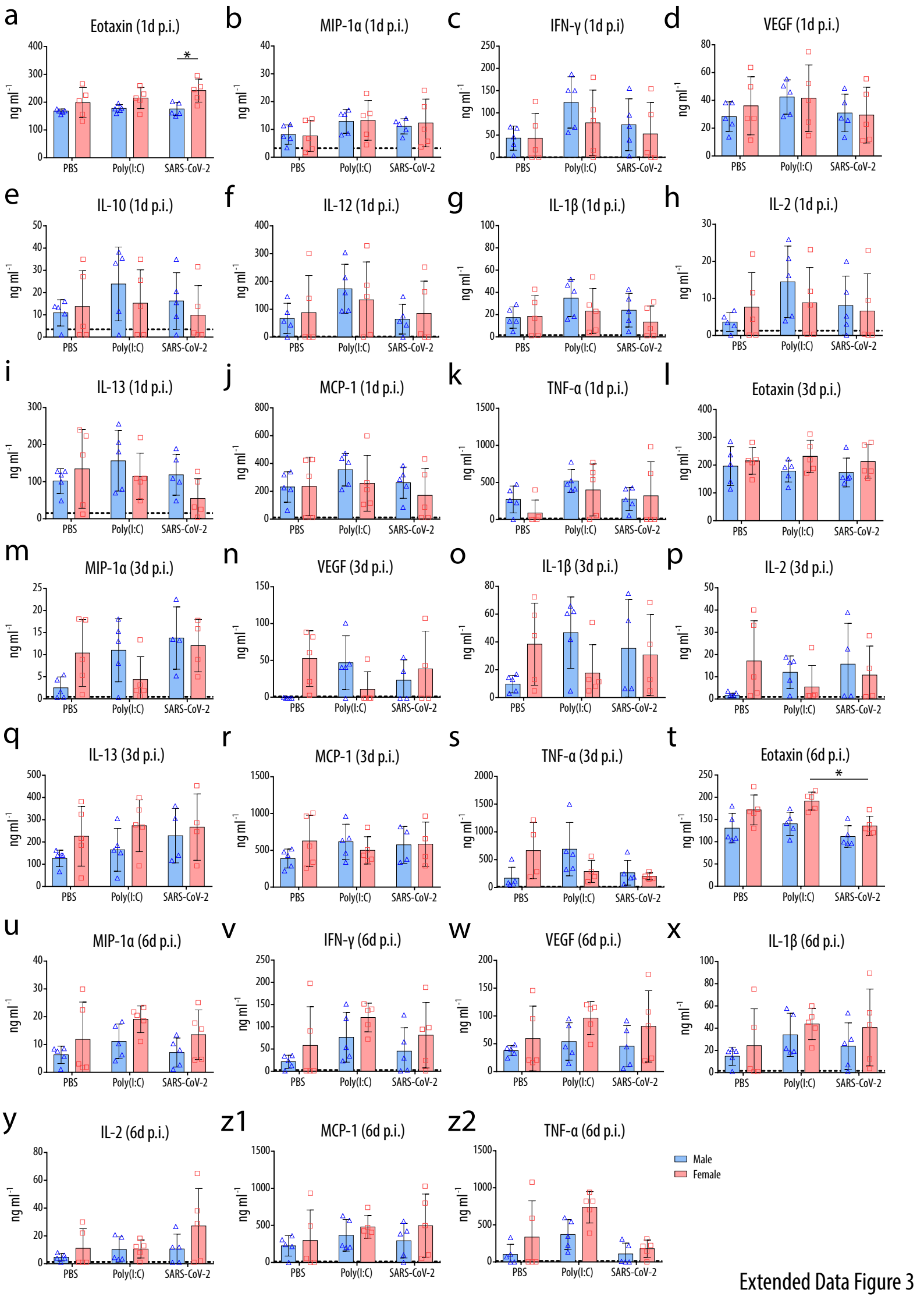

Extended Data Figure 3

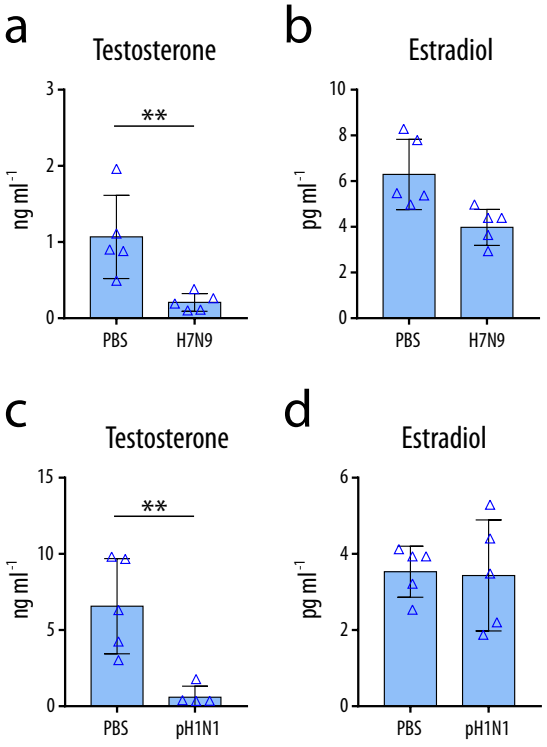

Extended Data Figure 4

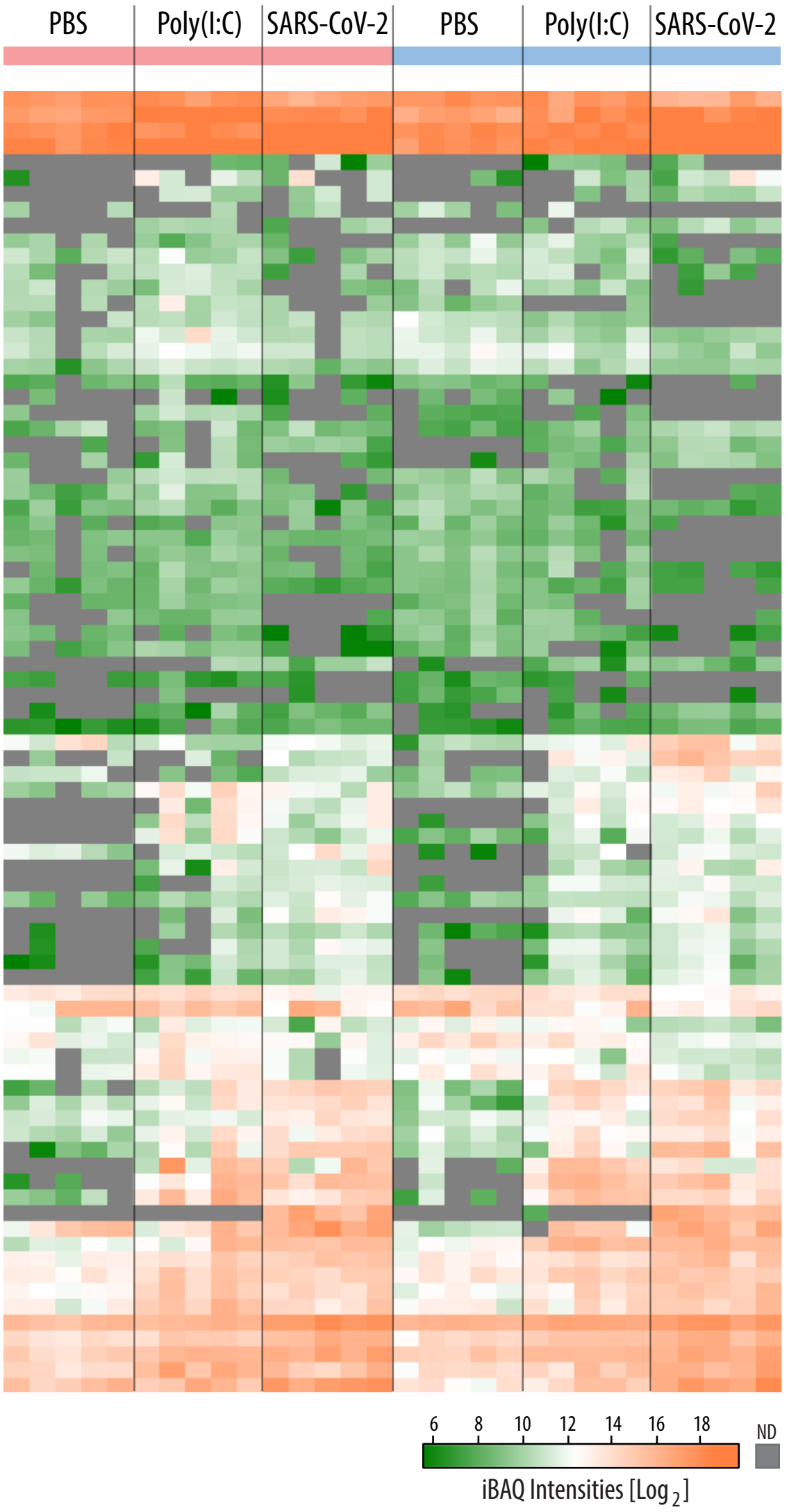

Extended Data Figure 5

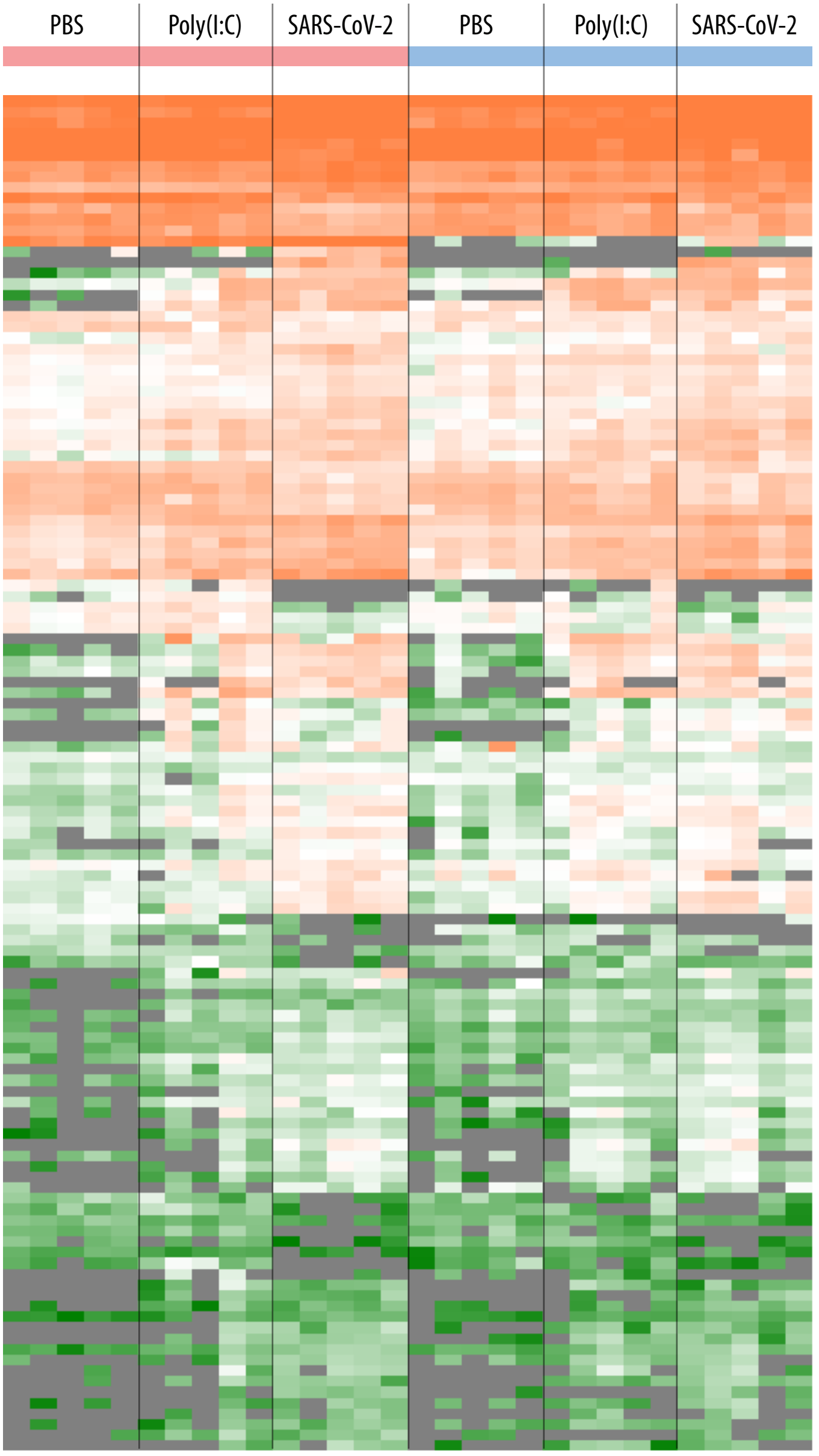

Extended Data Figure 6

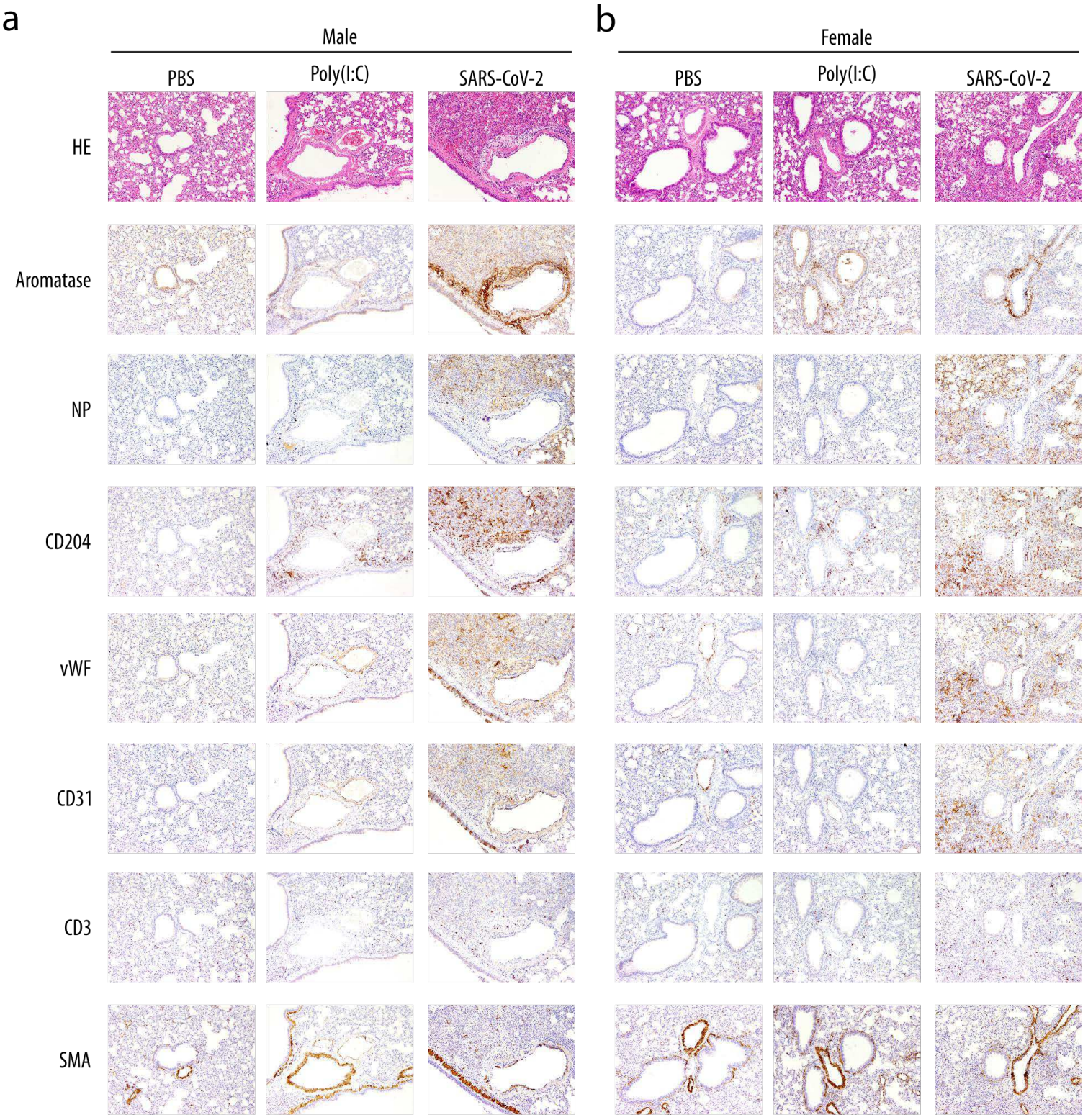

Extended Data Figure 7

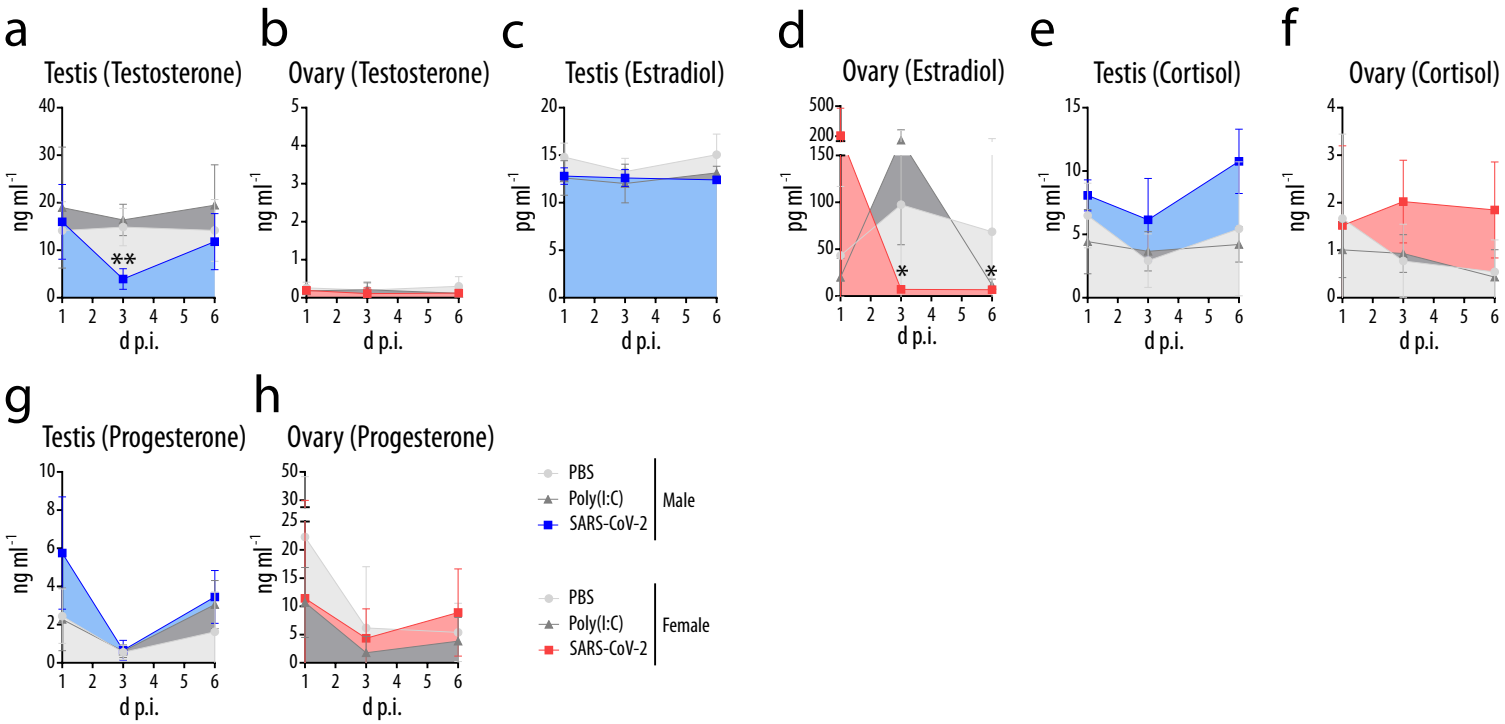

Extended Data Figure 8

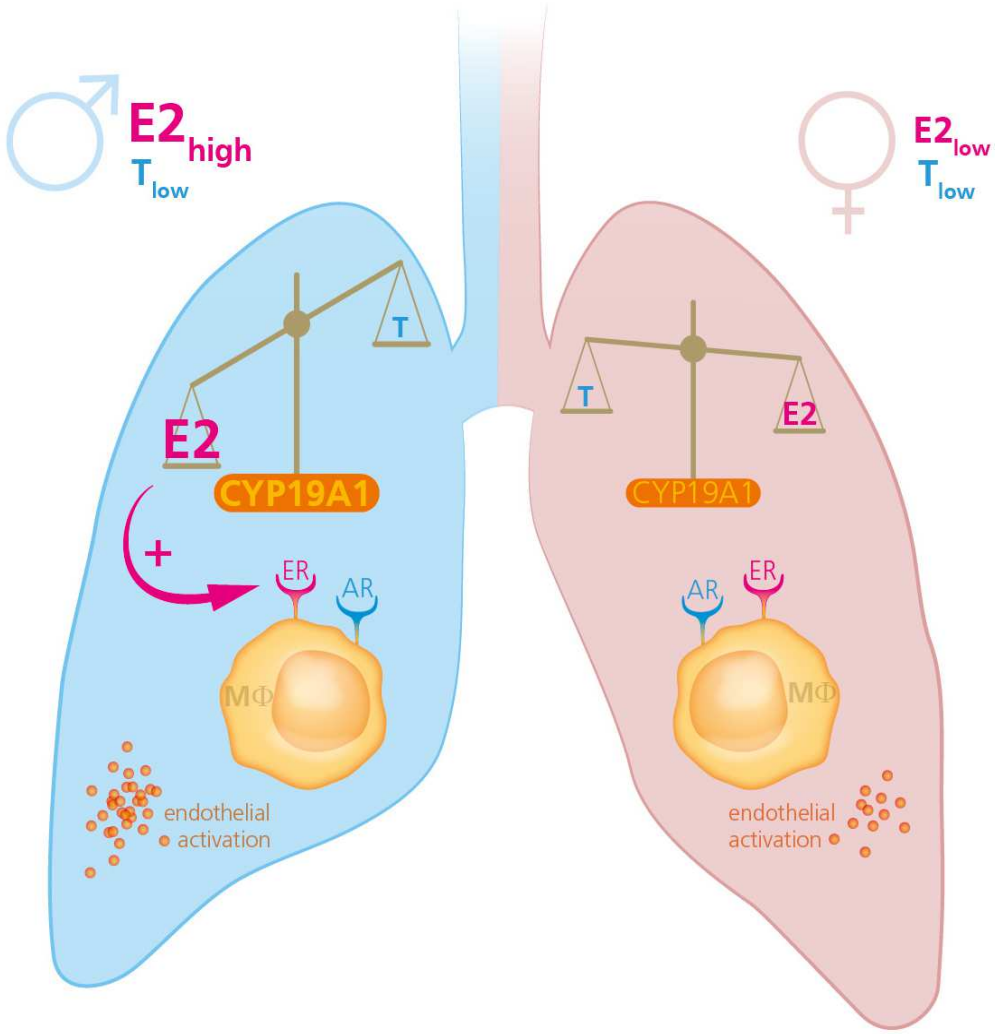

Extended Data Figure 9

Figures

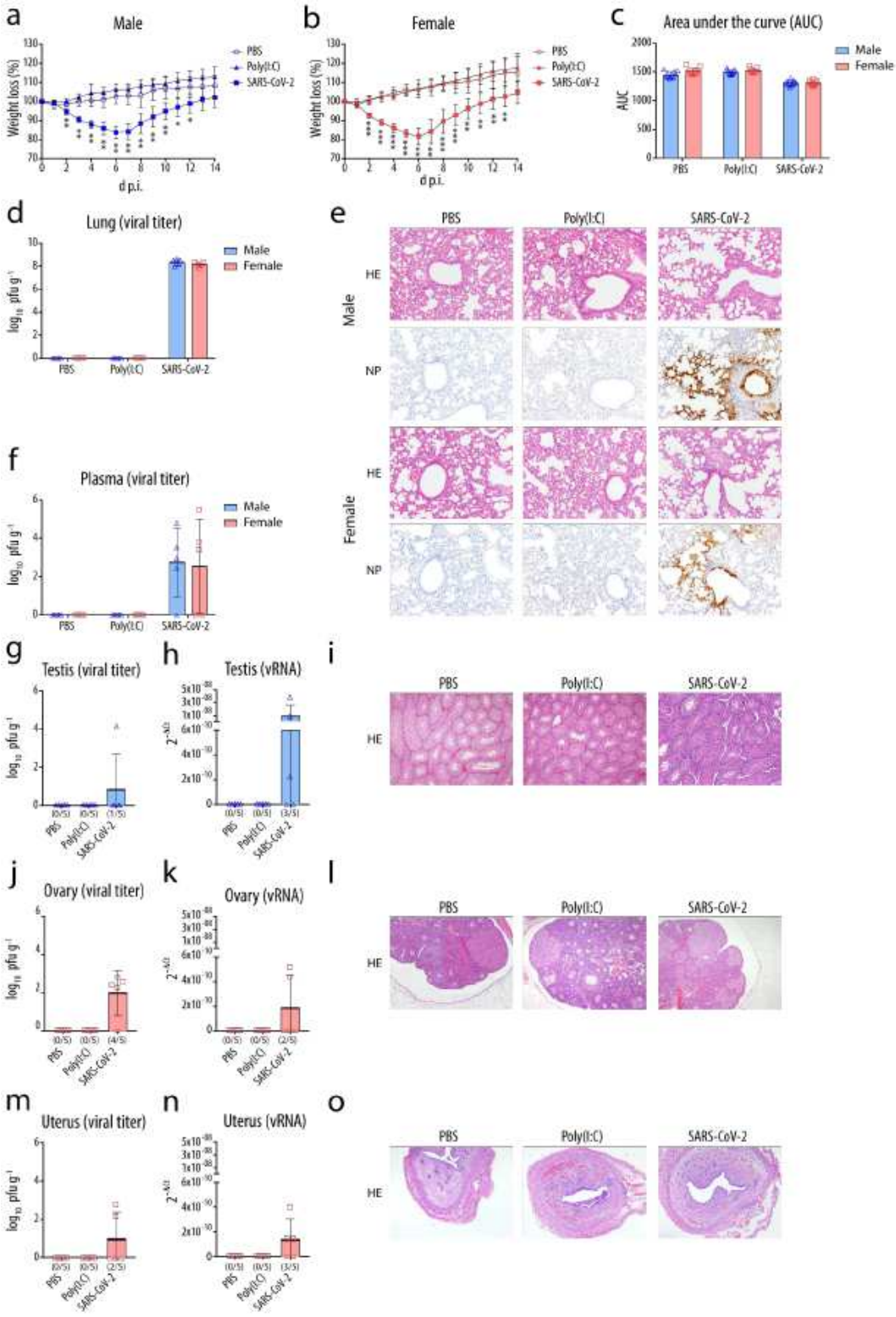

Figure 1

SARS-CoV-2 pathogenesis in male and female golden hamsters. a, b, Weight loss of male (a) and female (b) golden hamsters infected with SARS-CoV-2 (105 p.f.u. ml-1; male, n = 9; female n = 10), Poly(I:C) (n = 9) or PBS (n = 10). Statistical significance was assessed by Kruskal-Wallis one-way ANOVA (*p < 0.05,

**p<0.01, ***p<0.001). c, Area under the curve (AUC) for body weight of SARS-CoV-2 infected male and female golden hamsters. d, Viral lung titers of SARS-CoV-2 infected golden hamsters (3d p.i., n = 5). e, Haematoxylin and eosin (HE) and SARS-CoV-2 nucleoprotein (NP) staining in lungs of infected golden hamsters (3 dpi; representative pictures are shown, n = 5). f, Viral plasma titers of SARS-CoV-2 infected golden hamsters (3d p.i., n = 5). g, h, Viral titers (g) and viral RNA levels (h) in testis of male golden hamsters (3d p.i., n = 5). i, HE staining of testis from male golden hamsters (3d p.i., n = 5). j, k, Viral titers (j) and viral RNA levels (k) in ovary of female golden hamsters (3d p.i., n = 5). l, HE staining of ovary from female golden hamsters (3d p.i., n = 5). m, n, Viral titers (m) and viral RNA levels (n) in uteri of female golden hamsters (3d p.i., n = 5). o, HE staining in uteri of female Syrian golden hamsters (3d p.i., n = 5). a-d,f,g,h,j,k,m,n, Values are shown as means, error bars as SD.

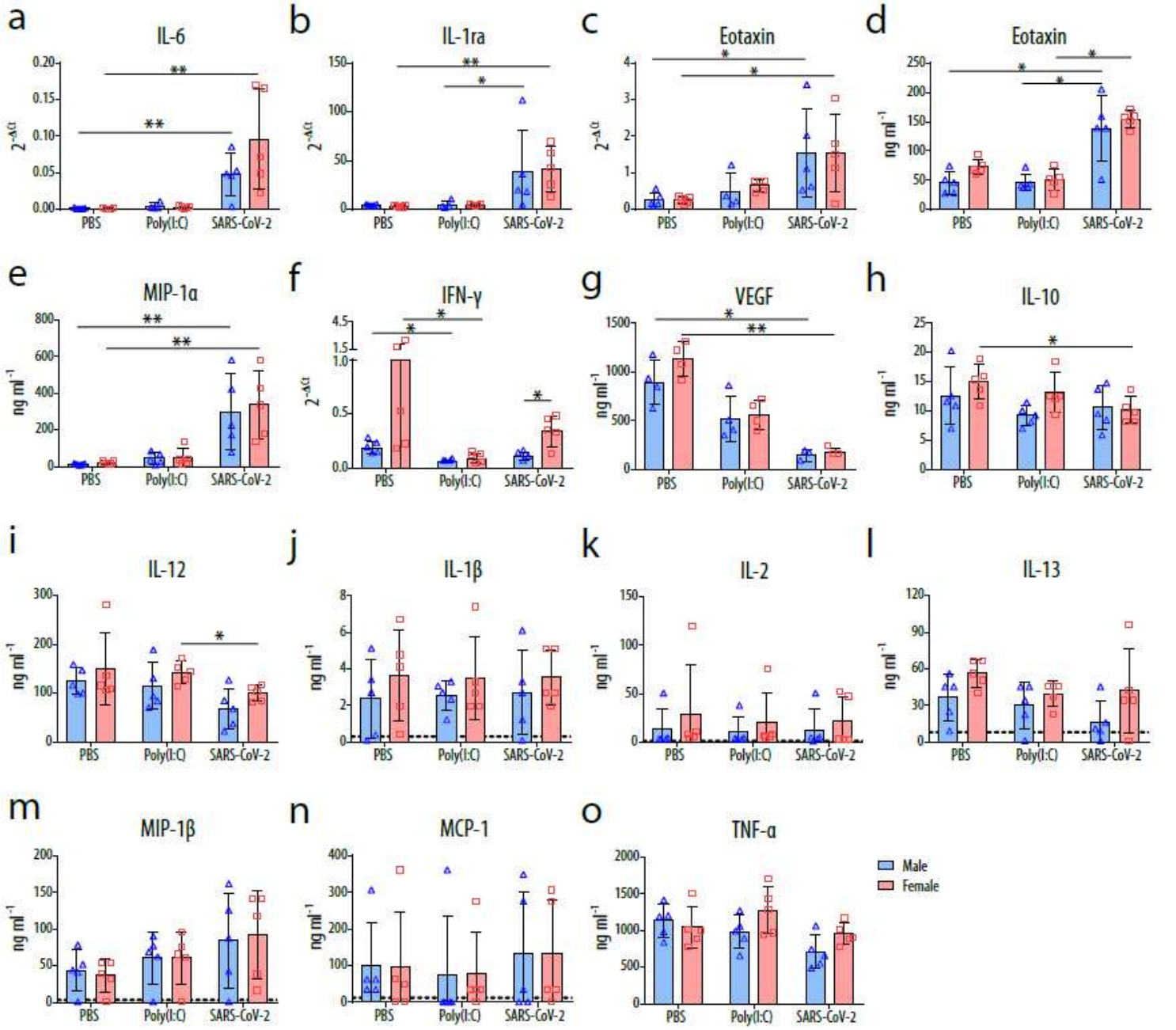

Figure 2

Immune response in the lungs of SARS-CoV-2 infected male and female golden hamsters. a, IL-6 mRNA expression levels (n = 5; male Poly(I:C): n = 4). b, IL-1ra mRNA expression levels (n = 5; male Poly(I:C): n = 4). c, d, Eotaxin mRNA (c) and protein (d) expression levels (n = 5; male Poly(I:C): n = 4). e, MIP-1α protein expression levels (n = 5). f, IFN-γ mRNA expression levels (n = 5; male Poly(I:C): n = 4). g, VEGF protein expression levels (n = 4; SARS-CoV-2: n = 3). h, IL-10 protein expression levels (n = 5). i, IL-12 protein expression levels (n = 5). j, IL-1β protein expression levels (n = 5). k, IL-2 protein expression levels (n = 5). l, IL-13 protein expression levels (n = 5). m, MIP-1b protein expression levels (n = 5). n, MCP-1 protein expression levels (n = 5). o, TNF-α protein expression levels (n = 5). Cytokine and chemokine levels were measured in lung homogenates at 3 d p.i.. Values are shown as means; error bars as SD; detection limits are indicated as dotted lines. Statistical significance was assessed by Kruskal-Wallis one-way ANOVA and by unpaired Student’s t test (*$p < 0.05$, **$p<0.01$).

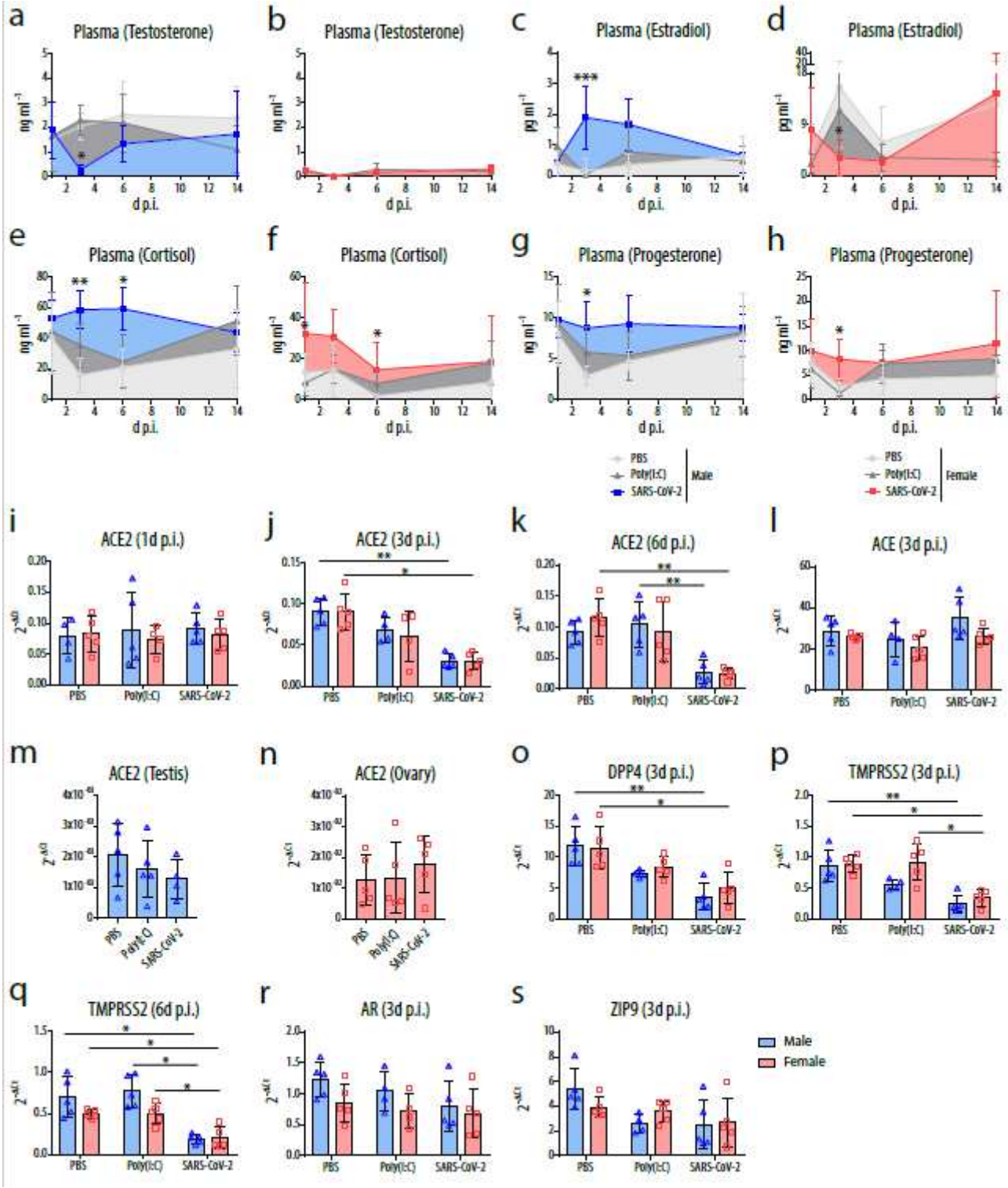

Figure 3

Sex hormones and SARS-CoV-2 entry receptors in infected male and female golden hamsters. a, b, Testosterone levels in plasma of male (a) and female (b) golden hamsters. c, d, Estradiol levels in plasma of male (c) and female (d) golden hamsters. e, f, Cortisol levels in plasma of male (e) and female (f) golden hamsters. g, h, Progesterone levels in plasma of male (g) and female (h) golden hamsters. Values are shown as means; error bars are shown as SD (n = 5; estradiol male3d p.i.: n = 10; estradiol male 14d p.i. SARS-CoV-2: n = 4; estradiol female 3d p.i. Poly(I:C) and SARS-CoV-2: each n = 8). i-k, ACE2 mRNA

expression levels at day 1 (i), 3 (j) and 6 (k) p.i. (n = 5; male Poly(I:C) 1d p.i.: n = 4; male and female Poly(I:C) 3d p.i.: n = 4) in the lungs of infected golden hamsters. l, ACE mRNA expression levels (n = 5; male Poly(I:C): n = 4) in the lungs of infected golden hamsters. m, n, ACE2 mRNA expression levels in testis of male (m) and ovary of female (n) golden hamsters at day 3 p.i. (n = 5; male SARS-CoV-2: n = 4). o, DPP4 mRNA expression levels (n = 5; male Poly(I:C): n = 4) in the lungs of infected golden hamsters. p, q, TMPRSS2 mRNA expression levels at day 3 (p) and 6 (q) p.i. in the lungs of infected golden hamsters. r, AR mRNA expression levels in the lungs of infected golden hamsters (n = 5; Poly(I:C): n = 4). s, ZIP9 mRNA expression levels in the lungs of infected golden hamsters (n = 5; male Poly(I:C): n = 4). The mRNA expression levels are presented as negative exponents of Δct values; values are shown as means; error bars are shown as SD. Statistical significance was assessed by Kruskal- Wallis one-way ANOVA (*$p < 0.05$, **$p < 0.01$, ***$p < 0.001$).

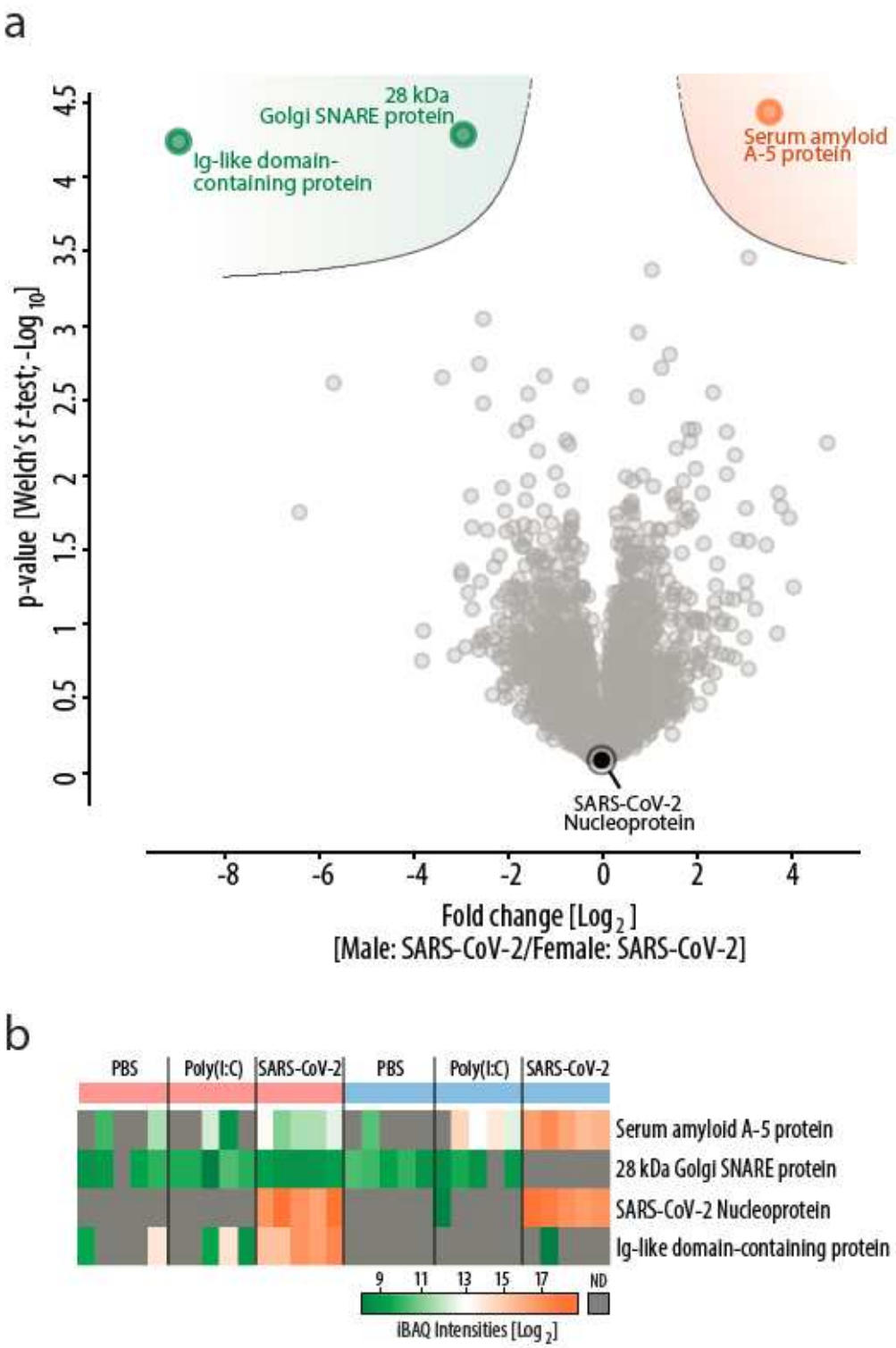

Figure 4

Proteomic analysis of the lungs of SARS-CoV-2 infected male and female golden hamsters. a, Volcano plot displaying host proteins up- or down-regulated in male versus female golden hamsters upon SARS-CoV-2 infection (orange and green dots, respectively). Significantly-regulated proteins are separated from background proteins by a hyperbolic curve (dotted grey line). b, Heatmap of iBAQ intensities for

significantly regulated proteins (Student's t-test, FDR 0.05, $p < 0.05$) in the total proteome across experimental groups and biological replicates.

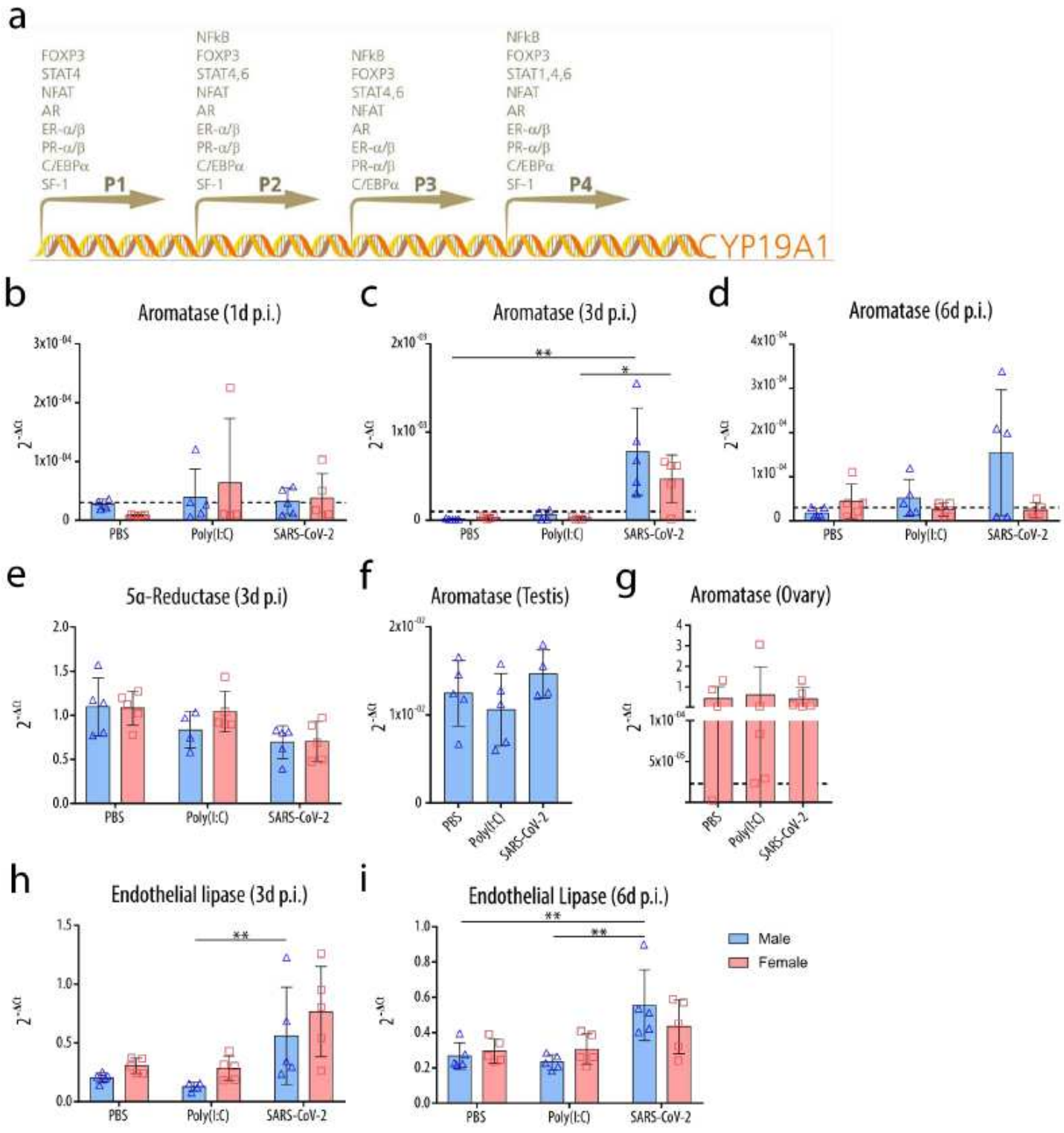

Figure 5

CYP19A1 and endothelial activation in the lungs of SARS-CoV-2 infected male and female golden hamsters. a, Schematic overview of binding sites for transcription factors in the four promoter regions (P1, P2, P3, and P4) of the aromatase gene CYP19A1. b-d, Aromatase mRNA expression levels at day 1

(b), 3 (c) and 6 (d) p.i. (n = 5; male Poly(I:C): n = 4). e, 5α-Reductase mRNA expression levels (n = 5; male Poly(I:C): n = 4). f, g, Aromatase mRNA expression levels in testis of male (f) and ovary of female (g) golden hamsters at 3d p.i. (n = 5; male SARS-CoV-2: n = 4). h, i, Endothelial lipase mRNA expression levels at day 3 (h) and 6 (i) p.i. (n = 5; male Poly(I:C) 3d p.i.: n = 4). The mRNA expression levels are presented as negative exponents of ct values; values are shown as means; error bars are shown as SD, detection limits are indicated as dotted lines. Statistical significance was assessed by Kruskal- Wallis one-way ANOVA (*p < 0.05, **p < 0.01).

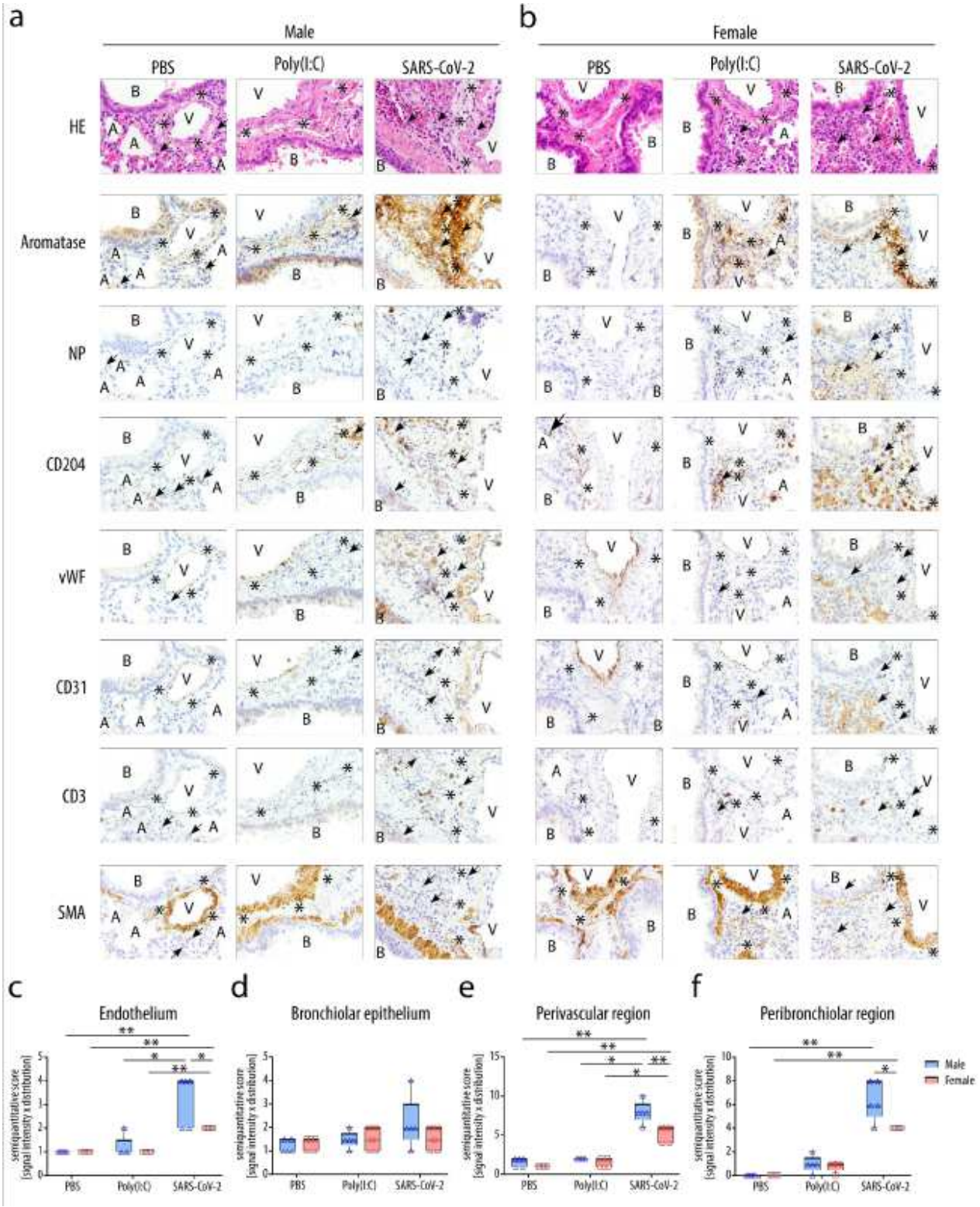

Figure 6

CYP19A1 protein expression in the lungs of SARS-CoV-2 infected male and female golden hamsters. a, b, Immunohistochemistry of serial sections from lungs of male (a) and female (b) golden hamsters for aromatase, SARS-CoV-2 NP, macrophages (CD204), endothelial cells (vWF and CD31), T cells (CD3) and smooth muscle (SMA). Bronchus (B), vessel (V), alveola (A), stars indicate perivascular connective tissue and arrowheads indicate macrophages. Representative pictures are shown. c-f Semiquantitative scoring of the of aromatase CYP19A1 immunoreactivity in different lung regions of male and female golden hamsters at day 3 p.i. (n = 5). Immunoreactivitiy was examined by light microscopy in the endothelium (c), the bronchiolar epithelium (d), the perivascular (e) and peribronchiolar region (f) in the lungs of infected hamsters. Signal intensity in respective regions was very low (0,5), low (1), low to moderate (2), moderate (3), moderate to high (4), or high (5). Signal distribution was assessed as: focal/oligofocal (≤3 foci; 1), multifocal (>3 foci; 2) and diffuse (3). For better comparative interpretation a final score for each region and animal was calculated as product of signal intensity times signal distribution. Statistical significance was assessed by Kruskal- Wallis one-way ANOVA and by unpaired Student's t-test (*$p < 0.05$, **$p<0.01$).

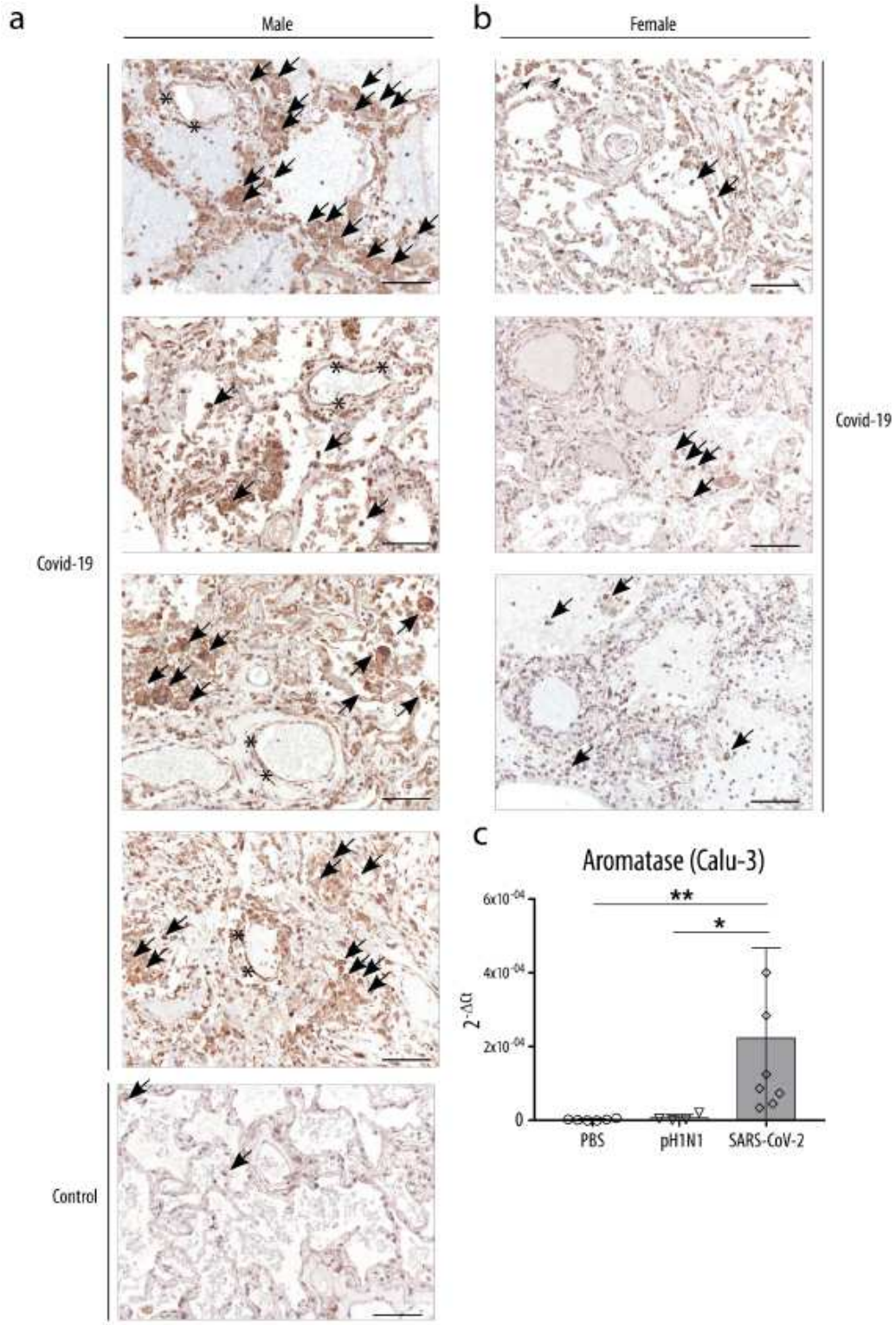

Figure 7

CYP19A1 protein expression in the lungs of fatal Covid-19 cases. Immunohistochemistry of lungs from male (a-d) and female (f-h) patients with Covid-19 or controls (e; representative picture of n = 3 are shown) stained for aromatase. The intensity of staining was significantly higher in endothelial cells and especially in macrophages in male (a d) compared to female (f-h) Covid-19 patients and control patients (e). Stars indicate endothelial cells and arrowheads indicate macrophages. Scale bar, 100 μm.